

Circumstellar molecular composition of the oxygen-rich AGB star IK Tau: II. In-depth non-LTE chemical abundance analysis

L. Decin^{1,2*}, E. De Beck¹, S. Brünken^{3,4}, H. S. P. Müller^{4,5}, K. M. Menten⁵, H. Kim^{5,6}, K. Willacy⁷, A. de Koter^{2,8},
and F. Wyrowski⁵

¹ Department of Physics and Astronomy, Institute of Astronomy, K.U.Leuven, Celestijnenlaan 200D, B-3001 Leuven, Belgium

² Sterrenkundig Instituut Anton Pannekoek, University of Amsterdam, P.O. Box 9429, 1090 CE Amsterdam, The Netherlands

³ Harvard-Smithsonian Center for Astrophysics, 60 Garden Street, Cambridge, MA 02138, USA

⁴ I. Physikalisches Institut, Universität zu Köln, Zùlpicher Street 77, 50937 Köln, Germany

⁵ Max-Planck Institut für Radioastronomie, Auf dem Hügel 69, 53121 Bonn, Germany

⁶ MPI für Gravitationsphysik, Calinstr. 38, 30167 Hannover, Germany

⁷ Jet Propulsion Laboratory, California Institute of Technology, Pasadena, CA 91109

⁸ Astronomical Institute, Utrecht University, Princetonplein 5, 3584 CC Utrecht, The Netherlands

Received January 26, 2010; accepted April 6, 2010

Abstract

Context. The interstellar medium is enriched primarily by matter ejected from evolved low and intermediate mass stars. The outflow from these stars creates a circumstellar envelope in which a rich gas-phase chemistry takes place. Complex shock-induced non-equilibrium chemistry takes place in the inner wind envelope, dust-gas reactions and ion-molecule reactions alter the abundances in the intermediate wind zone, and the penetration of cosmic rays and ultraviolet photons dissociates the molecules in the outer wind region.

Aims. Little observational information exists on the circumstellar molecular abundance stratifications of many molecules. Furthermore, our knowledge of oxygen-rich envelopes is not as profound as for the carbon-rich counterparts. The aim of this paper is therefore to study the circumstellar chemical abundance pattern of 11 molecules and isotopologs (¹²CO, ¹³CO, SiS, ²⁸SiO, ²⁹SiO, ³⁰SiO, HCN, CN, CS, SO, SO₂) in the oxygen-rich evolved star IK Tau.

Methods. We have performed an in-depth analysis of a large number of molecular emission lines excited in the circumstellar envelope around IK Tau. The analysis is done based on a non-local thermodynamic equilibrium (non-LTE) radiative transfer analysis, which calculates the temperature and velocity structure in a self-consistent way. The chemical abundance pattern is coupled to theoretical outer wind model predictions including photodestruction and cosmic ray ionization. Not only the integrated line intensities, but also the line shapes, are used as diagnostic tool to study the envelope structure.

Results. The deduced wind acceleration is much slower than predicted from classical theories. SiO and SiS are depleted in the envelope, possibly due to the adsorption onto dust grains. For HCN and CS a clear difference with respect to inner wind non-equilibrium predictions is found, either indicating uncertainties in the inner wind theoretical modeling or the possibility that HCN and CS (or the radical CN) participate in the dust formation. The low signal-to-noise profiles of SO and CN prohibit an accurate abundance determination; the modeling of high-excitation SO₂ lines is cumbersome, possibly related to line misidentifications or problems with the collisional rates. The SiO isotopic ratios (²⁹SiO/²⁸SiO and ³⁰SiO/²⁸SiO) point toward an enhancement in ²⁸SiO compared to results of classical stellar evolution codes. Predictions for H₂O emission lines in the spectral range of the Herschel/HIFI mission are performed.

Key words. Line: profiles, Radiative transfer, Stars: AGB and post-AGB, (Stars): circumstellar matter, Stars: mass loss, Stars: individual: IK Tau

1. Introduction

Asymptotic Giant Branch (AGB) stars are well known to release significant amounts of gas and dust in the interstellar medium via (copious) mass loss. This mass loss dominates the evolution of the star and ultimately, when the stellar envelope is exhausted, causes the star to evolve off the AGB into the post-AGB phase. The outflow from these evolved stars creates an envelope, which fosters gas-phase chemistry. The chemical complexity in circumstellar envelopes (CSEs) is thought to be dominated by the elemental carbon to oxygen ratio: oxygen-rich M-stars have

a C/O ratio less than unity, carbon-rich C-stars have C/O > 1, and for S-stars C/O is ~1.

Many have focused on the CSEs of carbon-rich stars in which a rich chemistry takes place. This is reflected by the detection of over 60 different chemical compounds, including unusual carbon chain radicals, in the CSE of IRC +10216, the prototype of carbon stars (e.g. Cernicharo et al. 2000). In contrast, only 10–12 compounds have been identified in the chemically most interesting oxygen-rich evolved stars, such as IK Tau and VY CMa (e.g. Ziurys et al. 2007). The first observations of carbon-bearing molecules (other than CO) in oxygen-rich AGBs were somewhat unexpected (e.g. Deguchi & Goldsmith 1985; Jewell et al. 1986). Nowadays, the formation of carbon molecules is thought to be the result of shock-induced non-equilibrium chemistry in the inner circumstellar envelope (e.g.

Send offprint requests to: L. Decin, e-mail: Leen.Decin@ster.kuleuven.ac.be

* Postdoctoral Fellow of the Fund for Scientific Research, Flanders

Duari et al. 1999) and/or a complex chemistry in the outer envelope triggered by the penetration of cosmic rays and ultra-violet radiation (e.g. Willacy & Millar 1997). Recently, a new interstellar molecule, PO ($X^2\Pi_r$), has been detected toward the envelope of the oxygen-rich supergiant VY CMa (Tenenbaum et al. 2007). Phosphorus monoxide is the first interstellar molecule detected that contains a P–O bond, a moiety essential in biochemical compounds. It is also the first new species identified in an oxygen-rich, as opposed to a carbon-rich, circumstellar envelope. These results suggest that oxygen-rich shells may be as chemically diverse as their carbon counterparts.

Circumstellar molecules have been extensively observed, both in the form of surveys of a single molecular species and in the form of searches for various molecular species in a limited number of carefully selected sources. The aim of these studies was to derive (*i.*) the mass-loss rate (from CO rotational lines) or (*ii.*) molecular abundances. For this latter purpose, several methods exist, each with varying degrees of complexity. (*1.*) For example, Bujarrabal et al. (1994) and Olofsson et al. (1998) showed that simple molecular line intensity ratios, if properly chosen, may be used to study the chemical behaviour in CSEs. The use of line intensity ratios has the advantage of requiring no assumptions about a circumstellar model, but it also limits the type of conclusions that can be drawn. (*2.*) Several authors have derived new constraints on chemical and circumstellar models based on the simplifying assumption of unresolved optically thin emission thermalized at one excitation temperature (e.g. Lindqvist et al. 1988; Omont et al. 1993; Bujarrabal et al. 1994; Kim et al. 2010). (*3.*) Later on, observations were (re)-analyzed based on a non-LTE (non local thermodynamic equilibrium) radiative transfer model (e.g. Bieging et al. 2000; Teyssier et al. 2006; Schöier et al. 2007a). In this study, we will go one step further and abandon or improve few of the assumptions still made in many non-LTE analyses.

1. Quite often, the temperature structure — being the most important factor determining the molecular line excitation — is approximated using a power-law (e.g. Bieging et al. 2000; Teyssier et al. 2006). Effects of different heating and cooling mechanisms are hence not properly taken into account. For instance, in the outermost parts of the envelope the temperature profile deviates from a power law distribution once the influence of photoelectric heating by the external interstellar radiation field becomes important (e.g. Crosas & Menten 1997; Justtanont et al. 1994; Decin et al. 2006).
2. The shell is often assumed to expand at a constant velocity (e.g. Bieging et al. 2000; Schöier et al. 2007a). However, for molecular lines primarily formed in the wind acceleration zone, the effect of a non-constant velocity structure on the derived molecular abundance may be significant.
3. The fractional abundances are estimated to follow an exponential or Gaussian distribution, assuming that the molecules are formed in the inner envelope, and photodissociated or absorbed onto dust grains further out (e.g. Bieging et al. 2000; González Delgado et al. 2003; Schöier et al. 2007a). The effect of extra formation and/or depletion processes in the envelope can hence not be taken into account.
4. Often, a maximum of two molecules (CO and one other) is analyzed at once (e.g. González Delgado et al. 2003; Schöier et al. 2007a).
5. Integrated line intensities are often used as a criterion to analyse the circumstellar chemical structure. However, line shapes provide us with strong diagnostic constraints to pin-

point the wind acceleration, which in turn has an influence on the deduced fractional abundances.

In this paper, we will study the circumstellar chemical abundance fractions of eleven different molecules and isotopologs in the oxygen-rich AGB star IK Tau based on the non-LTE radiative transfer code GASTRONOOM (Decin et al. 2006, 2007), which computes the temperature and velocity structure in the envelope in a self-consistent way. Chemical abundance stratifications are coupled to theoretical non-equilibrium (non-TE) predictions in the outer envelope by Willacy & Millar (1997) and compared to the shock-induced non-TE inner wind predictions by Duari et al. (1999) and Cherchneff (2006). IK Tau has been chosen for study because of the wealth of observations which are available for this target and the fact that its envelope is thought to be (roughly) spherically symmetric (Lane et al. 1987; Marvel 2005; Hale et al. 1997; Kim et al. 2010).

IK Tau, also known as NML Tau, was discovered in 1965 by Neugebauer et al. (1965). It is an extremely red Mira-type variable with spectral type ranging from M8.1 to M11.2 and a period around 470 days (Wing & Lockwood 1973). From dust shell motions detected at $11\ \mu\text{m}$ using the ISI interferometer, Hale et al. (1997) deduced a distance of 265 pc. This is in good agreement with the results of Olofsson et al. (1998) who computed a distance of 250 pc from integrated visual, near-infrared and IRAS data using a period-luminosity relation. Estimated mass-loss rates range from 3.8×10^{-6} (Neri et al. 1998) to $3 \times 10^{-5} M_{\odot}/\text{yr}$ (González Delgado et al. 2003). IK Tau's proximity and relatively high mass-loss rate (for a Mira) facilitates the observation of molecular emission lines.

In Sect. 2, we present the molecular line observational data used in this paper. Sect. 3 describes the background of the excitation analysis: the radiative transfer model used, the molecular line data and the theoretical ideas on molecular abundance stratification in the envelope. Sect. 4 describes the results: we first focus on the velocity structure in the envelope with special attention to the acceleration zone, after which the derived stellar parameters are discussed. Thereafter, the abundance structure for each molecule is derived and compared to the theoretical inner and outer wind predictions and observational results found in the literature. The time variability and SiO isotopic ratios are discussed in Sect. 5 and water line predictions are performed in Sect. 5.3. We end with some conclusions in Sect. 6.

2. Observational data

Part of the observations were obtained from our own observing programs scheduled at the JCMT, APEX and IRAM. These observations and the data reduction are described in Sect. 2.1. Other data are extracted from the literature and summarized briefly in Sect. 2.2. An overview is given in Table 1.

2.1. Observations and data reduction

The $^{12}\text{CO}(2-1)$, $^{12}\text{CO}(3-2)$, $^{12}\text{CO}(4-3)$ and the $^{13}\text{CO}(2-1)$ observations were extracted from the JCMT¹ archive. Additional data with the APEX² 12 m telescope were obtained for the $^{12}\text{CO}(3-2)$, $^{12}\text{CO}(4-3)$, $^{12}\text{CO}(7-6)$, and $^{13}\text{CO}(3-2)$ molecular

¹ The James Clerk Maxwell Telescope (JCMT) is operated by The Joint Astronomy Centre on behalf of the Science and Technology Facilities Council of the United Kingdom, the Netherlands Organisation for Scientific Research, and the National Research Council of Canada

² APEX, the Atacama Pathfinder Experiment, is a collaboration between the Max-Planck-Institut für Radioastronomie, the European

line transitions. With the 30 m telescope of the Institut de Radio Astronomie Millimétrique (IRAM)³ molecular line observations were performed in December 2006. During this observing run, data on the CO(2-1), SiS(8-7), SiS(12-11), SO₂(14_{3,11} - 14_{2,12}), SO₂(4_{3,1} - 4_{2,2}), SO₂(3_{3,1} - 3_{2,2}), SO₂(5_{3,3} - 5_{2,4}), and HCN(3-2)⁴ line transitions were obtained.

The JCMT and APEX observations were carried out using a position-switching mode. The IRAM observations were done in the wobbler-switching mode with a throw of 60". The frequency resolution for the JCMT-data equals 0.0305 MHz, for the APEX data it is 0.1221 MHz. The resolution was 1.25 MHz for the 3 and 2mm IRAM observations and 1 or/and 4 MHz at 1.3 and 1 mm, resulting in resolution slightly higher than 1 km/s for these observations.

The JCMT data reduction was performed with the SPLAT devoted routines of STARLINK, the APEX and IRAM data were reduced with CLASS. A polynomial of first order was fitted to an emission free region of the spectral baseline and subtracted. To increase the signal-to-noise ratio, the data were rebinned to a resolution of ~1 km/s so that we have at least 40 independent resolution elements per line profile. The antenna temperature, T_A^* , was converted to the main-beam temperature ($T_{mb} = T_A^*/\eta_{mb}$), using a main-beam efficiency, η_{mb} as specified in Table 1. The absolute uncertainties are ~20 %.

2.2. Literature data

To have better constraints on the chemical abundance pattern in the wind region around IK Tau, additional data were taken from the literature (see Table 1).

High-quality observations were performed by Kim (2006) with the APEX telescope in Chile during observing periods in November 2005, April 2006 and August 2006 (see also Kim et al. 2010, hereafter referred to as Paper I). In total, 34 transitions from 12 molecular species, including a few maser lines, were detected toward IK Tau.

Schöier et al. (2007b) published the observations of four SiS lines: the (5-4) and (6-5) rotational line transitions were obtained with the Onsala Space Observatory (OSO) telescope, the (12-11) and (19-18) rotational line observations were performed with the JCMT telescope.

SiO thermal radio line emission from a large sample of M-type AGB stars, including IK Tau, was studied by González Delgado et al. (2003). The SiO(2-1) line transition was obtained with the OSO telescope, the SiO(5-4) and (6-5) transitions with the Swedish ESO Submillimeterwave Telescope (SEST).

¹²CO line data were obtained by Teyssier et al. (2006) with the IRAM and JCMT telescope. The CO(1-0) line was observed by Ramstedt et al. (2008) in December 2003 with the 20 m OSO telescope. Olofsson et al. (1998) reported on the detection of the CS(2-1) line at 98 GHz with the OSO telescope with an integrated intensity of 0.5 K km/s.

³ IRAM is supported by INSU/CNRS (France), MPG (Germany), and IGN (Spain).

⁴ When the isotopic notation is not given, the molecular line transition is from the main isotopolog.

Table 1. Overview of the molecular line transitions used in this research, with indication of the frequency, the upper energy level, the telescope, the main beam half power beam width (HPBW) and main beam efficiency (η_{mb}).

Transition	Frequency [GHz]	E_{upper} [cm ⁻¹]	Telescope	HPBW (")	η_{mb}	Ref.
H¹²C¹⁴N						
3-2	265.886	17.7382	IRAM	9.5	0.46	1
4-3	354.505	29.5633	APEX	18	0.73	2
¹²C¹⁴N						
3 _{5/2} - 2 _{3/2}	340.032	22.6784	APEX	18	0.73	2
3 _{7/2} - 2 _{5/2}	340.248	22.7039	APEX	18	0.73	2
¹²C¹⁶O						
1-0	115.271	3.8450	IRAM	21	0.45	5
1-0	115.271	3.8450	OSO	33	0.43	6
2-1	230.538	11.5350	JCMT	20	0.69	1
2-1	230.538	11.5350	IRAM	10.5	0.57	1
3-2	345.796	23.0695	JCMT	14	0.63	1
3-2	345.796	23.0695	APEX	18	0.73	1
3-2	345.796	23.0695	APEX	18	0.73	2
4-3	461.041	38.4481	JCMT	11	0.52	1
4-3	461.041	38.4481	APEX	14	0.60	2
7-6	806.652	107.6424	APEX	8	0.43	2
¹³C¹⁶O						
2-1	220.398	11.0276	JCMT	20	0.69	1
3-2	330.588	22.0549	APEX	19	0.73	2
¹²C³²S						
6-5	293.912	34.3152	APEX	21	0.80	2
7-6	342.883	45.7525	APEX	18	0.73	2
²⁸Si¹⁶O						
2-1	86.846	4.3454	OSO	42	0.55	4
5-4	217.104	21.7261	SEST	25	0.55	4
6-5	260.518	30.4161	SEST	21	0.45	4
7-6	303.990	40.5540	APEX	20	0.80	2
8-7	345.061	52.1397	APEX	18	0.73	2
²⁹Si¹⁶O						
7-6	300.120	40.0461	APEX	20	0.80	2
8-7	342.980	51.4867	APEX	18	0.73	2
³⁰Si¹⁶O						
7-6	296.575	39.5730	APEX	20	0.80	2
8-7	339.930	50.8785	APEX	18	0.73	2
²⁸Si³²S						
5-4	90.771	9.0836	OSO	42	0.60	3
6-5	108.924	12.7169	OSO	35	0.50	3
8-7	145.226	21.7999	IRAM	17	0.69	1
12-11	217.817	47.2306	IRAM	10.5	0.57	1
12-11	217.817	47.2306	JCMT	22	0.70	3
16-15	290.380	82.3445	APEX	21	0.80	2
17-16	308.516	92.6355	APEX	20	0.80	2
19-18	344.779	115.0319	APEX	18	0.73	2
19-18	344.779	115.0319	JCMT	14	0.63	3
20-19	362.906	127.1372	APEX	18	0.73	2
³²S¹⁶O						
7 ₇ - 6 ₆	303.927	49.3181	APEX	20	0.80	2
8 ₈ - 7 ₇	344.310	60.8030	APEX	18	0.73	2
³²S¹⁶O¹⁶O						
14 _{3,11} - 14 _{2,12}	226.300	82.6982	IRAM	10.5	0.57	1
4 _{3,1} - 4 _{2,2}	255.553	21.7502	IRAM	9.5	0.46	1
3 _{3,1} - 3 _{2,2}	255.958	19.1968	IRAM	9.5	0.46	1
5 _{3,3} - 5 _{2,4}	256.247	24.9425	IRAM	9.5	0.46	1
3 _{3,1} - 2 _{2,0}	313.279	19.1968	APEX	20	0.80	2
17 _{1,17} - 16 _{0,16}	313.660	94.5810	APEX	20	0.80	2
4 _{3,1} - 3 _{2,2}	332.505	21.7502	APEX	19	0.73	2
13 _{2,12} - 12 _{1,11}	345.338	64.6273	APEX	18	0.73	2
5 _{3,3} - 4 _{2,2}	351.257	24.9425	APEX	18	0.73	2
14 _{4,10} - 14 _{3,11}	351.873	94.4354	APEX	18	0.73	2

References. (1) new data (see Sect. 2.1); (2) Kim et al. (2010); (3) Schöier et al. (2007b); (4) González Delgado et al. (2003); (5) Teyssier et al. (2006); (6) Ramstedt et al. (2008). 3

3. Excitation analysis

3.1. Radiative transfer model

The observed molecular line transitions provide information on the thermodynamic and chemical structure in the envelope around IK Tau. The line profiles were modeled with our non-LTE (non-Local Thermodynamic Equilibrium) radiative transfer code GASTRoNOoM (Decin et al. 2006). The code (1) calculates the kinetic temperature and velocity structure in the shell by solving the equations of motion of gas and dust and the energy balance simultaneously; then (2) solves the radiative transfer equation in the co-moving frame using the Approximate Newton-Raphson operator as developed by Schönberg & Hempe (1986) and computes the non-LTE level-populations; and finally (3) determines the observable line profile by ray-tracing. For a full description of the code we refer to Decin et al. (2006).

The main assumption of the code is a spherically symmetric wind. The mass-loss rate is allowed to vary with radial distance from the star. The local line width is assumed to be described by a Gaussian and is made up of a microturbulent component with a Doppler width of 1.5 km/s and a thermal component which is calculated from the derived kinetic temperature structure.

Two major updates have been made since the original publication in Decin et al. (2006).

- The code now iterates on steps (1) and (2) to obtain the kinetic temperature structure in a self-consistent manner from solving the energy balance equation, where the CO and H₂O line cooling (or heating) are directly obtained from the excitation analysis, i.e.

$$\Lambda = n_{\text{H}_2} \sum_l \sum_{u>l} (n_l \gamma_{lu} - n_u \gamma_{ul}) h \nu_{ul}, \quad (1)$$

where n_l and n_u are the level populations in the lower and upper levels participating in the transition at rest frequency ν_{ul} , and γ_{ul} and γ_{lu} are the CO-H₂ collisional rate coefficients. The cooling rate Λ (in erg s⁻¹ cm⁻³) is defined as positive for net cooling. In case of IK Tau the water line cooling dominates the CO line cooling by more than an order of magnitude in the inner wind region; for regions beyond 10¹⁶ cm the CO line cooling dominates over H₂O cooling with the adiabatic cooling being the dominant coolant agent.

- While the original version of the code approximates the stellar atmosphere with a blackbody at the stellar effective temperature, an additional option is now implemented to use MARCS theoretical model atmospheres and theoretical spectra (Gustafsson et al. 2008; Decin & Eriksson 2007) to estimate the stellar flux. Molecular species in the CSE, less abundant than CO and with larger dipole moments are primarily excited by infrared radiation from the central star (with the possible exception of HCN, Jura 1983, and H₂O, see Sect. 5.3). For CO, the infrared radiation competes with rotational excitation by collisions and by trapped rotational line photons to determine the populations of the rotational levels (Knapp & Morris 1985). For those minor species, the blackbody approximation of the stellar flux may lead to inaccurate absolute intensity predictions in the order of 5 to 20 %.

Decin et al. (2006, 2007) and Crosas & Menten (1997) demonstrated that not only the integrated line intensities, but particularly the line shapes should be taken into account for

a proper determination of the envelope structure. This is particularly true since (i.) the line shapes contain valuable information on the line forming region, e.g. a Gaussian line profile points toward line formation partially in the inner wind where the stellar winds has not yet reached its full terminal velocity (Bujarrabal & Alcolea 1991), and (ii.) while the absolute uncertainty of the intensity ranges between 20 to 50 %, the relative accuracy (of the line shapes) is of the order of a few percent. In contrast to most other studies, we therefore will not use a classical χ^2 -analysis using the integrated line intensity, but will perform the model selection and the assessment of goodness-of-fit using the log-likelihood function on the full line profiles as described in Decin et al. (2007).

3.2. Molecular line data

In this paper, line transitions of CO, SiO, SiS, CS, CN, HCN, SO, and SO₂ will be modeled, and H₂O line profile predictions for the Herschel/HIFI instrument will be performed. The molecular line data used in this paper are described in Appendix A.

3.3. Molecular abundance stratification

Theoretical chemical calculations clearly show that the fractional abundances (relative to H₂) vary throughout the envelope. Chemical processes responsible for the molecular content are dependent on the position in the envelope (see Fig. 1). In the stellar photosphere and at the inner boundary of the envelope, the high gas density and temperature ensure thermal equilibrium (TE). TE is suppressed very close to the photosphere because of the action of pulsation-driven shocks propagating outwards. Furthermore the regions of strong shock activity correspond to the locus of grain formation and wind acceleration. This region is referred to as the inner envelope (or inner wind) which extends over a few stellar radii. At larger radii (~ 5 to $100 R_*$) the newly formed dust grains interact with the cooler gas. Depletion or formation of certain molecular/atomic species may result from such an interaction and these layers are referred to as the intermediate envelope. This is also the region where parent molecules, injected in the envelope, may begin to break down, and daughter molecules are formed. At still larger radii ($>100 R_*$), the so-called outer envelope is penetrated by ultraviolet interstellar photons and cosmic rays resulting in a chemistry governed by photochemical processes.

Since our modeling results will be compared to chemical abundance predictions in the outer envelope by Willacy & Millar (1997) and in the inner envelope by Duari et al. (1999) and Cherchneff (2006), we first briefly describe these studies in Sect. 3.3.1 and Sect. 3.3.2 respectively. In Sect. 3.4 we discuss how we have implemented this knowledge in the modeling of the molecular line transitions.

3.3.1. Chemical stratification in the outer envelope

The chemistry in the outer envelope of IK Tau has been modeled by Willacy & Millar (1997). This chemical kinetic model aims at deriving the abundance stratification in the outer envelope (between 2×10^{15} and 2×10^{18} cm). The chemistry is driven by a combination of cosmic-ray ionization and ultraviolet radiation and starts from nine parent species injected into the envelope (see Table 2). The CSE of IK Tau was assumed to be spherically symmetric with a constant mass loss rate and a constant expan-

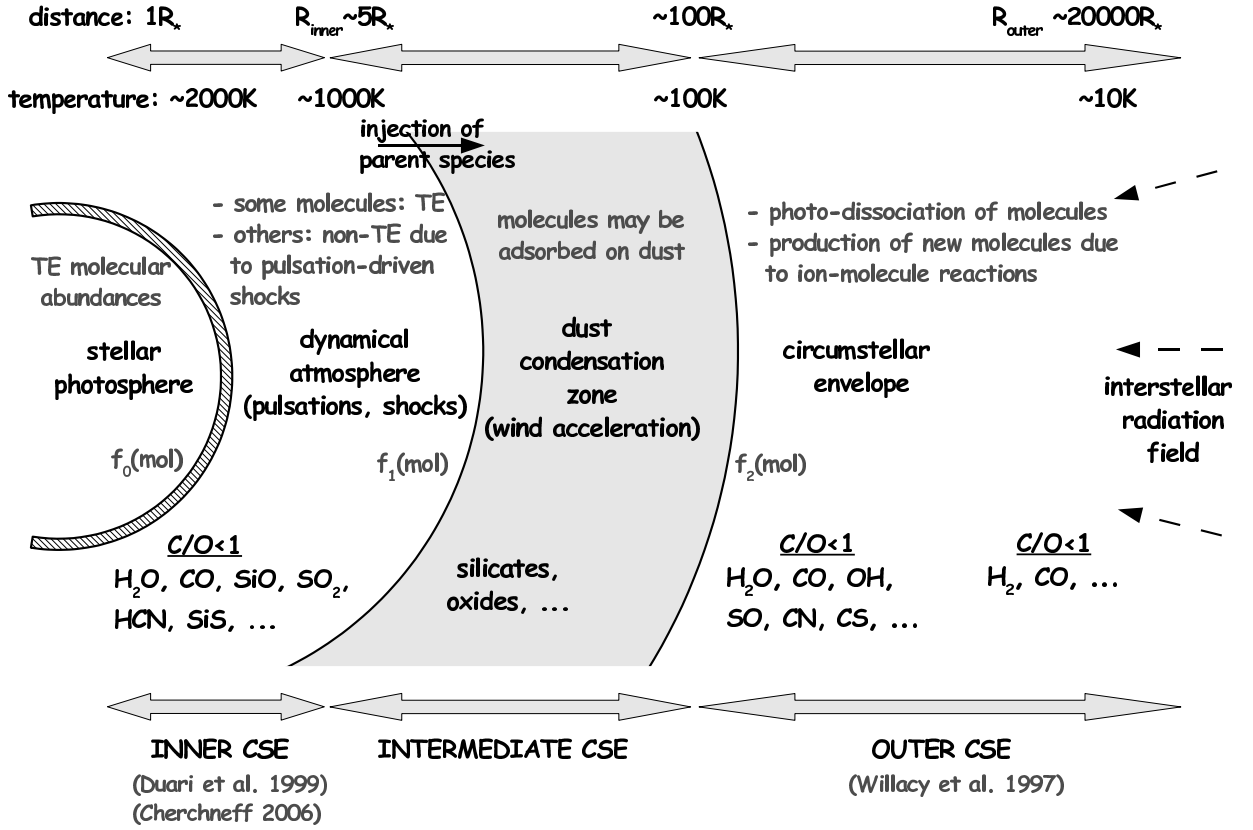


Figure 1. Schematic overview (not to scale) of the circumstellar envelope (CSE) of an oxygen-rich AGB star. Several chemical processes are indicated at the typical temperature and radial distance from the star in the envelope where they occur. The nomenclature as used in this paper is given.

sion velocity of 19 km/s. The temperature was described by a power law

$$T(r) = T(r_0) \left(\frac{r_0}{r} \right)^{0.6} \quad (2)$$

with $r_0 = 2 \times 10^{15}$ cm and $T(r_0)$ taken to be 100 K for $\dot{M} > 5 \times 10^{-6} M_{\odot}/\text{yr}$ and 300 K otherwise. For IK Tau $T(r_0)$ was assumed to be 100 K. The derived fractional abundances for the molecules studied in this paper are represented in Fig. 2.

Table 2. The fractional abundance (relative to H_2) taken for the parent species by Willacy & Millar (1997).

Parent species	Fractional abundance	Parent species	Fractional abundance
CO	4.00×10^{-4}	N_2	5.00×10^{-5}
H_2O	3.00×10^{-4}	H_2S	1.27×10^{-5}
CH_4	3.00×10^{-5}	SiS	3.50×10^{-6}
NH_3	1.00×10^{-6}	SiO	3.15×10^{-5}
He	1.00×10^{-1}	PH_3	3.00×10^{-8}
HCl	4.40×10^{-7}		

The model of Willacy & Millar (1997) succeeded in reproducing the observed values of certain species but failed for some other molecular abundances: the calculated abundance of HCN was too low and the injected abundance of the parent species SiS was about 10 times higher than observed. Duari et al. (1999) noted that the input molecular abundances of some parent species are sometimes questionably high since there exists no observational or theoretical evidence for the formation of these species in the inner and intermediate envelopes of O-rich Miras (see Sect. 3.3.2). More importantly, Duari et al. (1999) showed that HCN should form in the inner envelope or extended stellar atmosphere due to non-equilibrium shock chemistry, and may be a parent species injected to the outer envelope. Recent observational studies also indicate that HCN must be formed in the inner envelope (Bieging et al. 2000; Marvel 2005). These results are in contrast to the modeling efforts of Willacy & Millar (1997) where HCN was not yet considered as a parent species.

3.3.2. Chemical stratification in the inner envelope

Carbon-bearing molecules have been identified in the envelopes of many oxygen-rich AGB stars (e.g., Bujarrabal et al. 1994) and it was first thought that the observed carbon species were produced in the outer wind of O-rich stars via photochemical processes. However, Duari et al. (1999) showed that shock-induced

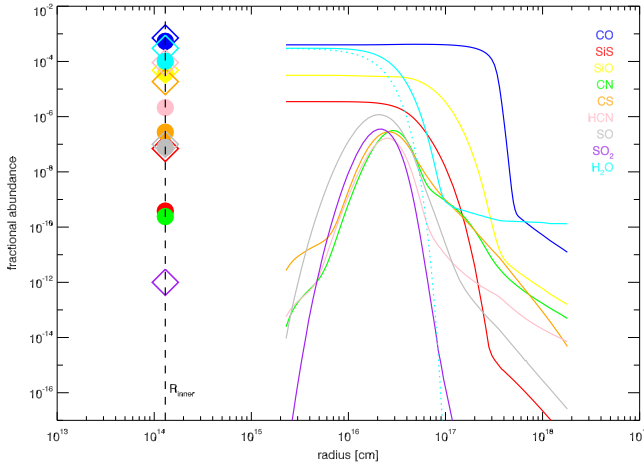


Figure 2. Theoretically predicted molecular abundance stratification in the envelope of IK Tau. The full lines represent the results as derived by Willacy & Millar (1997) for the outer envelope of IK Tau assuming a mass-loss rate of $1 \times 10^{-5} M_{\odot}/\text{yr}$. The diamonds represent the abundances derived by Cherchneff (2006) in the framework of non-equilibrium chemistry due to the passage of shocks in the inner envelope of TX Cam at $2 R_{\star}$; the filled circles indicate the results by Duari et al. (1999) for IK Tau at $2.2 R_{\star}$. The inner wind predictions are projected onto the dust-condensation radius derived in Sect. 4.1. The dotted line represents the Gaussian distribution of circumstellar H_2O as used by Maercker et al. (2008).

non-equilibrium chemistry models predict the formation of large amounts of a few carbon species, such as HCN, CS and CO_2 , in the inner envelope of IK Tau: these molecules are hence formed in the post-shocked layers and are then ejected in the outer wind as ‘parent’ species. For some parent species, the non-equilibrium chemistry does not alter significantly the initial photospheric TE abundances. But other species, abundant in the TE photosphere, are quickly destroyed in the outflow by the non-equilibrium chemistry generated by shocks (e.g., OH, SiS and HS). Again other species (such as SO) appear to be absent in the inner regions of the wind, and are thought to be produced by ion-molecule reactions in the photo-dissociation regions of the outer wind.

Cherchneff (2006) continued on the study of shock-induced non-equilibrium chemistry in the inner wind of AGB stars. She demonstrated that whatever the enrichment in carbon of the star (i.e. the C/O ratio), the atomic and molecular content after the passage of the first shock in the gas layers just above the stellar photosphere is very much the same, and in many cases, totally different from what would be expected from thermodynamic equilibrium (TE) calculations. In the case of the oxygen-rich envelope around TX Cam — being almost a stellar twin of IK Tau, but with slightly lower luminosity — Cherchneff (2006) found that while, e.g., the TE abundance of HCN (CS) is predicted to be $\sim 1.9 \times 10^{-11}$ ($\sim 2.5 \times 10^{-11}$), the non-TE fractional abundances at $2.5 R_{\star}$ are predicted to be $\sim 9 \times 10^{-5}$ ($\sim 1.85 \times 10^{-5}$). The fractional abundances derived by Cherchneff (2006) differ from the abundances of the injected parent molecules in the study of Willacy & Millar (1997) (see Table 2 and Fig. 2): Willacy & Millar (1997) did not consider CS and HCN as being parent molecules, and the (injected) abundance of SiS ($3.5 \times$

10^{-6}) is much higher than the abundance stratification derived by Cherchneff (2006) (see their Fig. 8).

3.4. Modeling strategy

3.4.1. Envelope structure as traced by the CO lines

The physical properties of the circumstellar gas, such as the temperature, velocity and density structure, are determined from the radiative transfer modeling of the multi-transitional (sub)millimetre CO line observations. Since higher- J lines are formed at higher temperature, different transitions offer the possibility to trace different regions in the envelope. The highest CO energy level traced is the CO $J^{\text{up}} = 7$ level at 154.8 K. The available rotational CO lines will hence be good tracers for the region beyond $\sim 100 R_{\star}$, but they do not put strong constraints on the temperature in the inner CSE. The upcoming Herschel/HIFI mission will be crucial in the study of the temperature structure in this inner wind region.

An extensive grid has been calculated with parameters ranging from 2000 to 3000 K for the stellar temperature T_{eff} , from 1×10^{13} to 6×10^{13} cm for the stellar radius R_{\star} , an inner (dust condensation) radius between 2 and $30 R_{\star}$, distance between 200 and 300 pc, and a constant mass-loss rate between 1×10^{-6} and $5 \times 10^{-5} M_{\odot}/\text{yr}$. As briefly explained in Sect. 3.1, a log-likelihood method (Decin et al. 2007) is used to find the best-fit model and derive a 95 % confidence interval for the model parameters. The results will be presented in Sect. 4.

3.4.2. Abundance stratification through the envelope

From the descriptions of theoretical abundance estimates in the inner and outer envelope (Sect. 3.3.1 – 3.3.2) it is clear that there is still some debate about the abundance structure in the envelope. SiS and HCN were already given as an example, but other molecules such as e.g. CS and SO also pose a problem. This is illustrated in Fig. 2, where one notices for a few molecules a large difference between the theoretically predicted fractional abundance in the inner envelope by Duari et al. (1999) and Cherchneff (2006) and the abundance of the parent molecules injected in the outer envelope by Willacy & Millar (1997). One of the big questions still existing concerns the modifications of the molecular abundances in the intermediate wind region due to gas-grain reactions. Currently, no theoretical efforts have been made to model this region in terms of molecular ‘leftovers’ after the dust formation has occurred. In the case of O-rich envelopes, it is thought that CO, HCN and CS are quite stable and travel the entire envelope unaltered until they reach the photo-dissociation region of the outer wind as these molecules do not participate in the formation of dust grains such as silicates and corundum (Duari et al. 1999). In contrast, SiO is a candidate molecule for depletion in the intermediate wind region due to the formation of SiO_2 (via a reaction with OH) whose condensation product, silica, is tentatively identified in post-AGB stars (Molster et al. 2002) and is claimed to be the carrier of the $13 \mu\text{m}$ feature in low mass-loss rate AGB stars (Speck et al. 2000, but other studies argue that this feature is due to spinel). The theoretical modeling of Duari et al. (1999) and Cherchneff (2006) predict an SiS abundance 2 to 3 orders of magnitude lower than the observed value, indicating that SiS is produced in the outer envelope of IK Tau. However, recent observational results by Decin et al. (2008b) argue for a formation process in the inner envelope.

From the above arguments, it is clear that we should allow some variation in modeling the abundance structure in the enve-

lope. However, one should also realize that we sometimes only have 2 rotational transitions of one isotopolog at our disposal with a restricted range in excitation temperature. The highest upper level energy traced is the SiS(20–19) transition at ~ 183 K; hence none of the studied transitions is sensitive to the abundance in the inner envelope ($R \lesssim 5 R_*$). In order to use some prior knowledge on the (theoretical) photo-dissociation rate in the outer regions and to allow for a depletion or an extra formation process in the intermediate/outer envelope, we therefore have opted to divide the envelope in different regimes (see also Table 3 and Fig 1): (i.) in the dust-free zone ($R \leq R_{\text{inner}}$) the abundance is constant ($f_1(\text{mol})$), (ii.) between R_{inner} and R_{max} the abundance can decrease/increase from $f_1(\text{mol})(R_{\text{inner}})$ to $f_2(\text{mol})(R_{\text{max}})$ linearly on a log-log scale, where both R_{max} and $f_2(\text{mol})$ are free parameters, (iii.) from R_{max} onwards, the abundance stratification follows the (photodissociation) results of Willacy & Millar (1997) scaled to $f_2(\text{mol})$ at R_{max} . In that way, 3 parameters ($f_1(\text{mol})$, $f_2(\text{mol})$, and R_{max}) have to be estimated to determine the abundance stratification of a species.

Table 3. Modeling assumptions of the abundance stratification.

Region	Variable	Comment
$R < R_{\text{inner}}$	$f_0(\text{mol})$	not sensitive
$R = R_{\text{inner}}$	$f_1(\text{mol})$	$f_0(\text{mol}) \equiv f_1(\text{mol})$
$R = R_2$	$f_2(\text{mol})$	allow for depletion (e.g. due to dust formation) or extra formation process
$R_{\text{inner}} < R < R_2$	R_2	linear interpolation in $\log(R)$ - $\log(f)$
$R > R_2$		theor. pred. of Willacy scaled to $f_2(\text{mol})$

Most studies use the photodissociation results of Mamon et al. (1988) to describe the CO spatial variation in the outer envelope. For other molecules, the abundance pattern is often assumed to be described by a simple Gaussian or exponential distribution (e.g. Bieging et al. 2000; González Delgado et al. 2003; Schöier et al. 2007b). The e -folding radius then describes the photodissociation by ambient UV photons penetrating the dusty envelope or depletion of the molecules from the gas into dust grains in the outflowing stellar wind. That way, however, all molecules are assumed to be created in the extended atmosphere or inner wind region. Moreover, a combination of depletion and photodissociation or extra depletion/formation processes in the intermediate/outer region can not be captured, and one can not use the results by Willacy & Millar (1997) describing extra formation of a few molecules by ion-ion reactions in the outer wind region. The methodology outlined above (Table 3) captures these flaws, and may serve to considerably strengthen our knowledge on the abundance stratification in the envelope.

As was already alluded to in the previous paragraph, the line profiles in this study are not sensitive to a change in abundance in the inner wind region ($R \leq R_{\text{inner}}$). To assess the abundance stratification in this region, one either needs high-resolution near-infrared (see, e.g., Decin et al. 2008a) or far-infrared spectroscopy (as will be provided by the Herschel/HIFI instrument). Nonetheless, the derived abundance stratifications will be compared to the theoretical inner wind predictions by Duari et al. (1999) and Cherchneff (2006), since this comparison may yield hints on the (un)reactivity of the molecules in the dust forming region and on uncertainties in the inner wind predictions.

4. Results

Using the log-likelihood method, the parameters for the model yielding the best-fit to the CO line profiles are derived (see parameters listed in the 2nd column in Table 4, ‘model 1’). The CO lines, however, only trace the envelope beyond $\sim 100 R_*$. One therefore should use other molecules to put constraints on the structure in the inner wind region. HCN is the only molecule for which we have observational evidence that it is formed in the inner wind region: using interferometric data Marvel (2005) deduced a maximum size for the HCN distribution of $3.85''$ (in diameter), or a radius of 7.2×10^{15} cm at 250 pc. They concluded that the deduced size indicates a shock origin for HCN close to the star and a radius for the HCN distribution limited by photodissociation. The HCN line profiles (Fig. 7) are clearly Gaussian indicating a line formation (at least partly) in the inner wind region, where the wind has not yet reached its terminal velocity. That way, HCN observations yield important clues on the velocity structure in the inner wind region. Using the stellar parameters as given in the 2nd column in Table 4 (‘model 1’), we were unable to derive a HCN-abundance structure yielding a satisfactory fit to the line profiles. While the integrated intensities could be well predicted, the line profiles were flat-topped with a FWHM (full width at half maximum) being too large. The only way to reconcile this problem was (1) concentrating the HCN abundance in the inner 2×10^{15} cm with $[\text{HCN}/\text{H}] = 9 \times 10^{-6}$, or (2) allowing for a smoother velocity law. While the abundance in the former solution is within the predictions of Cherchneff (2006), the angular distance is much smaller than the $3.85''$ diameter deduced by Marvel (2005).

4.1. Velocity structure

The expansion velocity of SiO, H₂O, and OH masers can be used to put further constraints on the velocity structure, and specifically on the acceleration in the inner wind region (see Fig. 3). It is clear that the velocity structure as derived from the parameters of the best-fit model only based on CO lines (model 1), is far too steep in the inner wind region as compared to the velocity indications of the maser lines. This problem can be solved by either increasing the dust condensation radius or by allowing for a smoother velocity profile. This latter can be simulated using the classical β -law (Lamers & Cassinelli 1999) with $\beta > 0.5$ (see Fig. 3)

$$v(r) \simeq v_0 + (v_\infty - v_0) \left(1 - \frac{R_*}{r}\right)^\beta \quad (3)$$

with v_0 the velocity at the dust condensation radius.

One should realize that several assumptions are inherent to the velocity structure derived from solving the momentum equation: (i.) All dust species at all different grain sizes are assumed to be directly formed at the dust condensation radius R_{inner} . However, theoretical results from, e.g., Gail & Sedlmayr (1999) show that formation and growth of (silicate) dust grains typically occur between 1100 and 900 K, i.e. extending over a few stellar radii. (ii.) The extinction efficiencies used in the GASTRoNOoM-code represent the Fe-rich silicate MgFeSiO₄. Thanks to their high absorption efficiencies at optical and near-infrared wavelength Fe-rich silicates like MgFeSiO₄ (and solid Fe) are efficient wind drivers (Woitke 2006). However, other oxides or pure silicates such as Al₂O₃, SiO₂, Mg₂SiO₄ and MgSiO₃ have low absorption efficiencies at optical and near-infrared wavelengths, resulting in a negligible radiative pressure on all glassy condensates. If these latter molecules were the

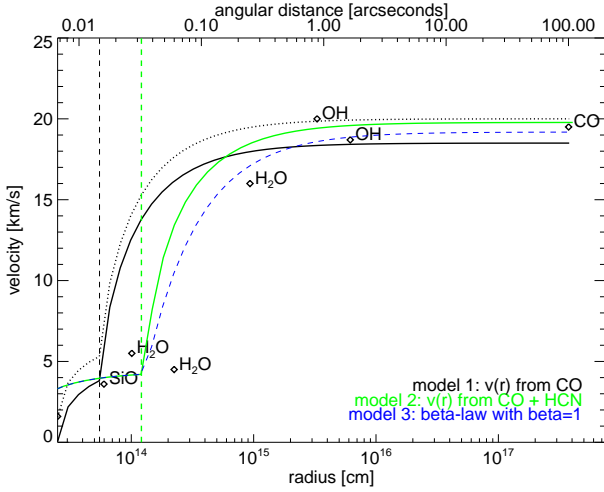


Figure 3. Velocity profile of IK Tau. Velocity data are obtained from mapping of maser emission: SiO (Boboltz & Diamond 2005), H₂O (Bains et al. 2003), and OH (Bowers et al. 1989). The CO expansion velocity derived from our CO data is also indicated. The expansion velocity deduced from the CO data alone (see ‘model 1’ in Table 4) is plotted as full black line. The dotted black line indicates the velocity structure taking a turbulent velocity (of 1.5 km/s) into account. The green line gives the expansion (+turbulent) velocity deduced from both the CO and HCN lines (model 2 in Table 4). The dashed blue line represents an even smoother expansion (+turbulent) velocity structure, applying Eq. 3, with $\beta = 1$ (model 3 in Table 4). The vertical dashed black and green lines indicate the dust condensation radius R_{inner} . Note that $\beta=0.5$ in the inner wind region.

most abundant in the envelope of IK Tau, the wind acceleration would be much lower. No medium resolution infrared (from the Infrared Space Observatory - Short Wavelength Spectrometer or the Spitzer - InfraRed Spectrograph) data are, however, available for IK Tau, hence we were unable to study the circumstellar dust composition in detail. (iii.) ‘Complete momentum coupling’ is assumed. This means that the grain motion everywhere in the flow can be computed by equating the local radiative and collisional drag forces implying that virtually all of the momentum gained by a grain through the absorption of radiation from the stellar photosphere is transferred via collisions to the atmospheric gas (MacGregor & Stencel 1992). For physical conditions typical of the circumstellar envelopes of oxygen-rich red giants, MacGregor & Stencel (1992) find that silicate grains with initial radii smaller than about $5 \times 10^{-2} \mu\text{m}$ decouple from the ambient gas near the base of the outflow. (iv.) The momentum equation used in the GASTRoNoM-code (see Eq. 2 in Decin et al. 2006), implicitly assumes that the mass outflow is steady in time and that the circumstellar dust is optically thin to the stellar radiation (Goldreich & Scoville 1976). Dust emission modeling by Ramstedt et al. (2008) suggests a circumstellar envelope which is slightly optically thick at $10 \mu\text{m}$ ($\tau_{10} = 1.2$). These results suggest that the acceleration of the gaseous particles in the inner wind might be slower than deduced from solving the momentum equation (‘model 1’ and ‘model 2’), since not all dust species take part in the momentum transfer.

Solving the momentum equation and taking both the CO and HCN line profiles into account, the inner radius of the dusty envelope is shifted towards higher values, $R_{\text{inner}} = 1.3 \times 10^{14}$ cm, and the mass-loss rate slightly increases (‘model 2’ in Table 4).

Using the same stellar parameters as in ‘model 2’, but simulating a smoother velocity law still compatible with the maser line mapping ($\beta = 1$) decreases the mass-loss rate to $8 \times 10^{-6} M_{\odot}/\text{yr}$ (model 3 in Table 4), due to the condition of mass conservation (model 3 in Table 4). The narrow Gaussian line profiles of the HCN lines (Sect. 4.3.2) give more support to model 3 than to model 2, for which reason the thermodynamic structure as deduced from model 3 (Fig. 4) will be used to model the other molecular line transitions.

4.2. Stellar parameters derived from the CO and HCN lines

The stellar parameters for the best-fit model (model 3) are listed in Table 4. The outer radius of CO is computed using the results of Mamon et al. (1988). The derived 95% confidence intervals in Table 4 are statistical uncertainties, which should be interpreted in the light of the model assumptions of a spherically symmetric wind. As described in Decin et al. (2007), the log-likelihood function can also be used to compare different models with a different number of parameters. In case of IK Tau, we have assessed the likelihood preference of a model with constant mass-loss rate compared to a model with mass-loss rate variations. The preferences pointed towards the simpler model, i.e. with a constant mass-loss rate (of $8 \times 10^{-6} M_{\odot}/\text{yr}$). We also derived the dust-to-gas mass ratio from the amount of dust needed to drive a wind at a terminal velocity of 17.7 km/s for a gas mass-loss rate of $8 \times 10^{-6} M_{\odot}/\text{yr}$ with the deduced velocity profile. A dust-to-gas mass ratio of 1.9×10^{-2} (or a dust mass-loss rate of $1.52 \times 10^{-7} M_{\odot}/\text{yr}$) is obtained for model 3, with an estimated uncertainty of a factor ~ 5 .

4.3. Fractional abundances

Using the thermodynamic envelope structure derived above (see Fig. 4), the abundance stratification of all molecules is derived. A comparison to the theoretical inner and outer wind predictions (as discussed in Sect. 3.3.1–3.3.2) is given in Fig. 5. The studied molecular line transitions are not sensitive to the full envelope size, but have a limited formation region. The part in the envelope we can trace by combining the different available rotational line transitions is indicated with vertical dashes in Fig. 5 and tabulated in Table 5⁵.

A comparison between observed and predicted line profiles and a discussion on the deduced abundance stratification are given for each molecule separately in the following subsections. We will always first briefly describe the deduced abundances, then compare the results to the theoretical inner and outer wind predictions and finally compare to other results found in the literature (see Table 6). For the literature results, a difference is made between studies based on the assumptions of optically thin unresolved emission and a population distribution thermalized at an excitation temperature that is constant throughout the envelope, and those based on a full non-LTE radiative transfer calculation. One should also realize that most studies make use of integrated line intensities, and do not deal with a full line profile analysis as is done here. With the exception of Omont et al. (1993), the other literature studies listed in Table 6 assume the shell to expand at a constant velocity. As discussed in Sect. 4.1, the Gaussian line profiles of the HCN and a few of the SiO lines are the result

⁵ Estimates of these ranges are found by considering the place where $I(p)p^3$, with I the intensity and p the impact parameter, is at half of its maximum value.

Table 4. Parameters of the models with best goodness-of-fit for IK Tau. Details for each model are given in the text. The numbers in italics are input parameters that have been kept fixed at the given value.

based on $v(r)$	model 1 CO momentum eq.	model 2 CO & HCN momentum eq.	model 3 CO & HCN power-law $\beta = 1$	95% confidence interval for model 3
parameter	value	value	value	
T_{eff} [K]	2200	2200	2200	100
R_{\star} [10^{13} cm]	2.5	1.5	1.5	1.0
[CO/H ₂] [10^{-4}]	2	2	2	—
distance [pc]	250	265	265	20
R_{inner} [R_{\star}]	2.2	8.7	8.7	2
R_{outer} [R_{\star}]	15170	27000	27000	—
v_{∞} [km s^{-1}]	17.7	17.7	17.7	—
$\dot{M}(r)$ [M_{\odot}/yr]	8×10^{-6}	9×10^{-6}	8×10^{-6}	1×10^{-6}
$^{12}\text{C}/^{13}\text{C}$	20	16	14	2

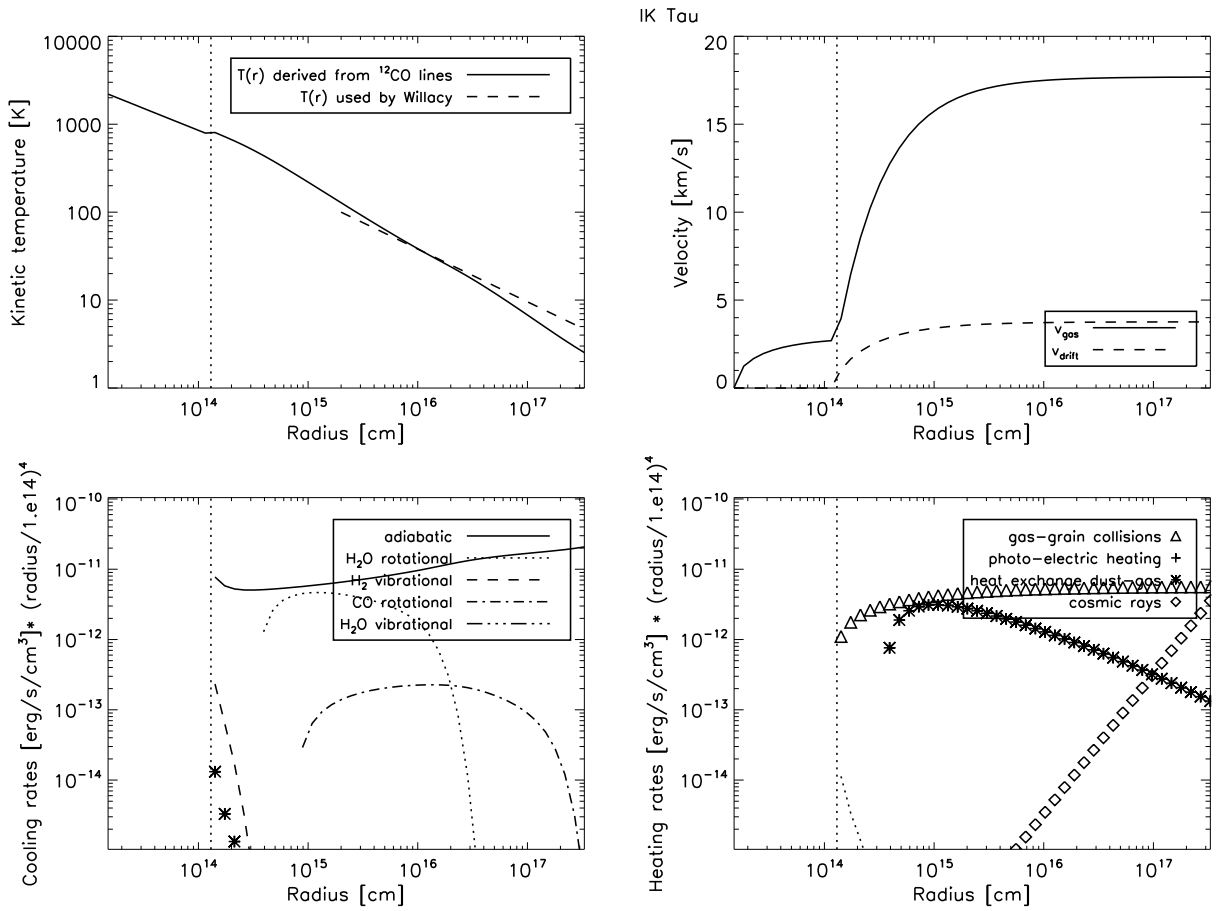


Figure 4. Thermodynamic structure in the envelope of IK Tau as derived from the ^{12}CO and HCN rotational line transitions for the stellar parameters of model 3 in Table 4. *Upper left:* Estimated temperature profile, *upper right:* estimated gas and drift velocity, *lower left:* cooling rates, and *lower right:* heating rates. The start of the dusty envelope, R_{inner} , is indicated by the dotted line. The temperature structure as used in the chemical kinetic calculations by Willacy & Millar (1997) is plotted in the upper left panel in dashed lines.

of line formation partially in the inner wind, where the stellar wind has not yet reached its full terminal velocity. As a result, more emission is produced at velocities near the line center than would be the case for a uniform-velocity wind. Hence, obser-

vational studies assuming a constant expansion velocity, will be unable to predict the line profiles properly.

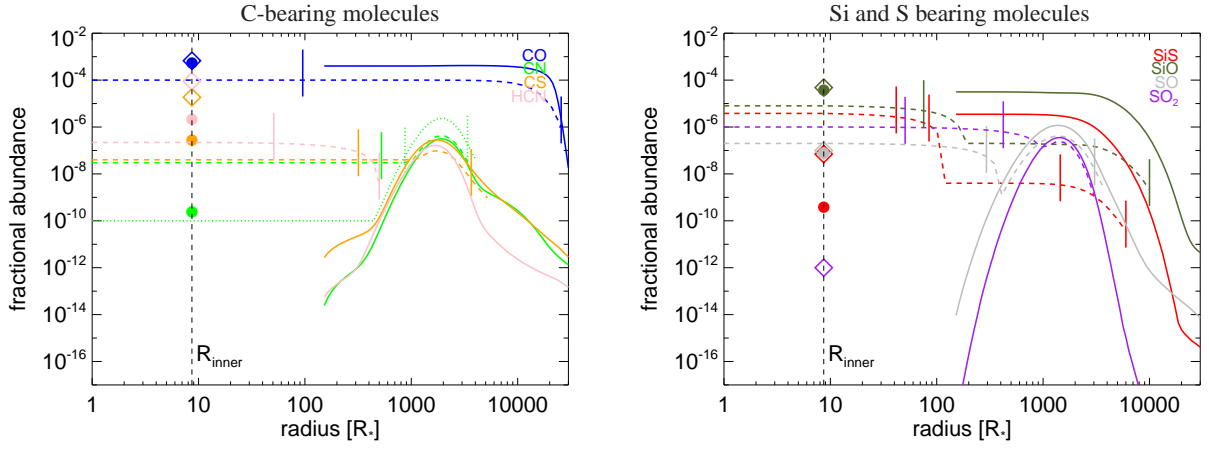


Figure 5. Predicted abundance stratifications [mol/ H_{tot}] (full line, see Fig. 2) are compared to the deduced abundance structures (dashed lines). In the left panel, the carbon bearing molecules are shown, the right panel gives the Si and S bearing molecules. For CN, an alternative solution is given in dotted lines. For each molecule, the line formation region traced by the observed molecular lines is indicated by the vertical dashes (see also Table 5).

Table 5. Molecular fractional abundance relative to $H_{\text{tot}}=n(\text{H})+2n(\text{H}_2)$ (see Fig. 5).

	$f_1(\text{mol})$	$f_2(\text{mol})$	$R_2 [R_\star]$	ranges $[R_\star]$
^{12}CO	1.0×10^{-4}	1.0×10^{-4}	25170	100–25000
^{13}CO	7.1×10^{-6}	7.1×10^{-6}	25170	500–15000
SiS	5.5×10^{-6}	4.0×10^{-9}	120	40–80, 1500–6000
^{28}SiO	8.0×10^{-6}	2.0×10^{-7}	180	70–10000
^{29}SiO	3.0×10^{-7}	7.5×10^{-9}	180	70–2000
^{30}SiO	1.0×10^{-7}	2.5×10^{-9}	180	70–2000
CS	4.0×10^{-8}	4.0×10^{-8}	1160	300–4000
SO	2.0×10^{-7}	1.0×10^{-9}	400	200–3000
SO ₂	1.0×10^{-6}	1.0×10^{-7}	1000	50–400
HCN	2.2×10^{-7}	4.0×10^{-9}	500	50–500
CN	3.0×10^{-8}	3.0×10^{-8}	1000	500–3500
<i>alternative solution</i>				
CN	1.0×10^{-10}	1.0×10^{-10}	450	900–3500

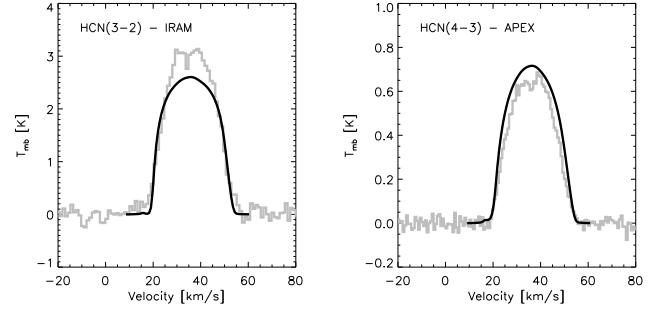


Figure 7. HCN observed spectral lines (gray) are compared to the spectral line predictions (black) based on the CSE model shown in Fig. 4 and the abundance stratification displayed in Fig. 5.

4.3.1. CO

Results: A comparison between the observed rotational ^{12}CO and ^{13}CO lines and theoretical predictions is shown in Fig. 6. The ^{12}CO and ^{13}CO lines are very well reproduced by the GASTRoNOoM-predictions, both in integrated intensities and in line shapes. Only the IRAM $^{12}\text{CO}(1-0)$ and $^{12}\text{CO}(2-1)$ lines are slightly over-predicted. It is, however, not the first time that the non-compatibility of the IRAM absolute flux level is reported (see, e.g. Decin et al. 2008a; Schöier et al. 2006).

Comparison to theoretical predictions: The CO fractional abundance assumed in all observational studies (see also Table 6) is always lower than the deduced inner wind theoretical non-TE values of Duari et al. (1999) and Cherchneff (2006). The non-TE theoretical values are comparable to the TE-value of 6.95×10^{-4} at $1 R_\star$ (Duari et al. 1999). Increasing the CO fractional abundance by a factor 5, would decrease the mass-loss rate by a factor ~ 2.8 to reproduce the observed CO rotational line profiles (using the scaling laws deduced by De Beck et al. 2010).

Comparison to other observational studies: Most observational studies listed in Table 6 assume a fractional CO abundance of $[\text{CO}/\text{H}] = 1 - 1.5 \times 10^{-4}$. Using different CO rotational lines the mass-loss rate is then derived. The deduced $^{12}\text{CO}/^{13}\text{CO}$ ratio ranges between 9 and 14.

Using CO rotational line transitions, other studies have also estimated the mass-loss rate (see Table 7). The results depend on the assumed or derived temperature distribution, the distance, the adopted $[\text{CO}/\text{H}_2]$ abundance ratio, and the radiative transfer model or analytical approximation used. All (scaled) mass-loss rate values are in the narrow range between 6.5×10^{-6} and $9 \times 10^{-6} M_\odot/\text{yr}$, the exception being the result of González Delgado et al. (2003), which is a factor ~ 4 higher. We note that the work of these authors was not devoted to the study of CO, and it remains unclear what line intensities they used in their modeling.

4.3.2. HCN

Results: The narrow Gaussian line profiles clearly point toward (at least) an inner wind origin of HCN. As discussed above, we impose a value $R_2 = 500 R_\star$ to simulate the mapping re-

Table 6. Comparison of the deduced fractional abundances to other observational studies and theoretical predictions. All fractional abundances are given relative to the total H-content. In cases where values found in literature were given relative to H₂, they were re-scaled relative to the total H-content by assuming that all hydrogen is in its molecular form H₂.

	¹² CO	¹³ CO	CS	HCN	CN	SiO	SiS	SO	SO ₂
Lindqvist et al. (1988) ^a	1.5×10^{-4}	—	1.5×10^{-7}	3.0×10^{-7}	—	—	3.5×10^{-7}	—	—
Omont et al. (1993) ^b	—	—	—	—	—	1.5×10^{-6}	—	9×10^{-7}	2.05×10^{-6}
Bujarrabal et al. (1994) ^c	1.5×10^{-4}	1.6×10^{-5}	5.0×10^{-8}	4.9×10^{-7}	—	8.5×10^{-6}	2.2×10^{-7}	1.3×10^{-6}	—
Kim et al. (2010) ^d ('case A')	1.5×10^{-4}	1.75×10^{-5}	3.0×10^{-7}	1.4×10^{-6}	1.6×10^{-7}	1.3×10^{-5}	1.3×10^{-6}	7.8×10^{-7}	1.4×10^{-5}
Kim et al. (2010) ^d ('case B')	1.5×10^{-4}	1.75×10^{-5}	8.1×10^{-8}	4.3×10^{-7}	5.1×10^{-8}	5.1×10^{-6}	3.1×10^{-7}	2.7×10^{-7}	4.2×10^{-6}
González Delgado ^e et al. (2003)	1.0×10^{-4}	—	—	—	—	2.0×10^{-7}	—	—	—
Schöier et al. (2007a) ^f	1.0×10^{-4}	—	—	—	—	—	5×10^{-6} -5.0×10^{-9}	—	—
this work	1.0×10^{-4}	7.1×10^{-6}	4×10^{-8}	2.2×10^{-7}	1.0×10^{-10} -3.0×10^{-8}	8.0×10^{-6} -2.0×10^{-7}	5.5×10^{-6} -4.0×10^{-9}	2.0×10^{-7}	1.0×10^{-6}
Duari et al. (1999) ^h	5.38×10^{-4}	—	2.75×10^{-7}	2.12×10^{-6}	2.40×10^{-10}	3.75×10^{-5}	3.82×10^{-10}	7.79×10^{-8}	—
Cherchneff (2006) ⁱ	6.71×10^{-4}	—	1.85×10^{-5}	9.06×10^{-5}	3×10^{-11g}	4.80×10^{-5}	7×10^{-8}	1×10^{-7}	1×10^{-12}
Willacy & Millar (1997) ^j	4×10^{-4}	—	2.9×10^{-7}	1.4×10^{-7}	3.5×10^{-7}	3.2×10^{-5}	3.5×10^{-6}	9.1×10^{-7}	2.2×10^{-7}

Notes. In the first part of the table, observational results are listed based on the assumption of optically thin emission and a population distribution which is thermalized at one excitation temperature. The second part gives observational results based on a non-LTE radiative transfer analysis. Theoretical predictions for either the inner envelope (Duari et al. 1999; Cherchneff 2006) or outer envelope (Willacy & Millar 1997) fractional abundances are given in the last part.

References.

^a: no information on used distance and mass-loss rate

^b: distance is 270 pc, $\dot{M} = 4.5 \times 10^{-6} M_{\odot}/\text{yr}$

^c: distance is 270 pc, $\dot{M} = 4.5 \times 10^{-6} M_{\odot}/\text{yr}$

^d: distance is 250 pc, assumed \dot{M} of $4.7 \times 10^{-6} M_{\odot}/\text{yr}$, LTE is assumed, 'case B' represents a solution with a larger outer radius than 'case A'

^e: r_e in Gaussian distribution for SiO is 2.5×10^{16} cm, distance is 250 pc and $\dot{M} = 3 \times 10^{-5} M_{\odot}/\text{yr}$

^f: r_e in Gaussian distribution for SiS, distance is 260 pc and $\dot{M} = 1 \times 10^{-5} M_{\odot}/\text{yr}$. For 2-component model: f_c is 5.5×10^{-6} and taken constant out to 1.0×10^{15} cm and the lower abundance Gaussian component has f_0 of 5.0×10^{-9} and r_e of 1.6×10^{16} cm. Using one (Gaussian) component distribution, f_0 is 5×10^{-8} and r_e is 1.6×10^{16} cm.

^g: only value at $5 R_{\star}$ is given

^h: predicted values at $2.2 R_{\star}$ in the envelope for IK Tau

ⁱ: predicted values at $2 R_{\star}$ in the envelope for TX Cam

^j: predicted peak fractional abundances in the outer envelope

sults of Marvel (2005). The deduced abundance around $50 R_{\star}$ is $[\text{HCN}/\text{H}] = 2 - 2.5 \times 10^{-7}$.

Comparison to theoretical predictions: Theoretical predictions by Duari et al. (1999) and Cherchneff (2006) and observational studies by, e.g., Bieging et al. (2000) and Marvel (2005) indicate that HCN forms in the inner wind region of M-type envelopes by shock-induced non-equilibrium chemical processes. This is contrary to the photochemical models of Willacy & Millar (1997), where HCN is only produced in the outer envelope by photochemical reactions involving NH₃ and CH₃, which they assumed to be parent species originating close to the stellar photosphere and injected in the outer region. This formation route, however, leads to line shapes which are clearly non-Gaussian but are flat-topped (for optically thin unresolved emission) since the wind is already at its full velocity in this region.

The maximum size distribution of $3.85''$ derived by Marvel (2005) is suggested to be caused by photodissociation of HCN. Bieging et al. (2000) used a parametrized formula to describe the photodissociation radius for HCN as a function of gas mass-loss rate and wind velocity (see their Eq. 2). This estimate leads to a HCN photodissociation radius of 1.2×10^{16} cm, in good

agreement with the result of Marvel (2005) of 7.6×10^{15} cm (at 265 pc). Using HCN as a parent species with an injected abundance of 1.5×10^{-7} , new chemical outer wind models were calculated using the code as described in Willacy & Millar (1997). The derived photodissociation radius is around 2×10^{16} cm, being a factor ~ 3 higher than the observed value of Marvel (2005).

Compared to the theoretical predictions for TX Cam at $5 R_{\star}$ by Cherchneff (2006) or for IK Tau at $2.2 R_{\star}$ by Duari et al. (1999), our deduced abundance is a factor 10 to 40 lower, respectively. There are a few possibilities for the origin of this difference. (i.) Contrary to what is thought (e.g. Duari et al. 1999), HCN may participate in the formation of dust grains in the inner envelope. (ii.) The formation mechanism of HCN in the inner wind is directly linked to its radical CN by



The destruction route is the reverse reaction. Shocks trigger CN and further HCN formation in the gas (Cherchneff 2006). The formation processes of both molecules depend critically on the physical parameters of the shocked gas, specifically on the physics in the 'very fast chemistry zone', that is the narrow region after the shock front itself. The modeling of this zone is still subject to many uncertainties (e.g. cooling rate, velocity,

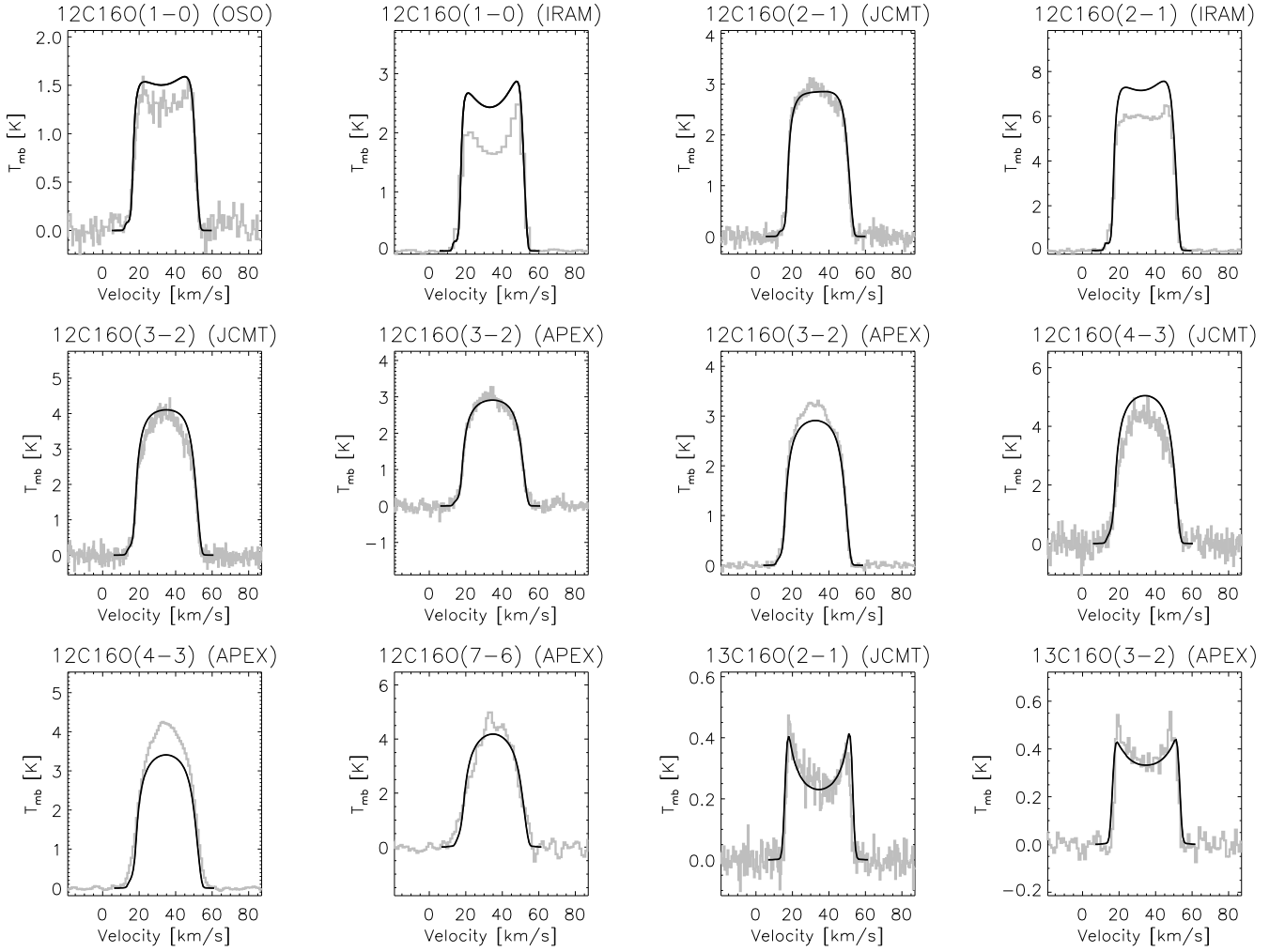


Figure 6. CO rotational line profiles of IK Tau (plotted in grey) are compared with the GASTRoNOoM non-LTE line predictions (in black) using the parameters of ‘model 3’ as specified in Table 4. The rest frame of the velocity scale is the local standard of rest (LSR) velocity.

shock strength), yielding uncertainties on the theoretical fractional abundances of at least one order of a magnitude.

Comparison to observational studies: All observational deduced values agree within a factor ~ 2 , but are clearly lower than the inner wind non-TE theoretical predictions (see Table 6).

4.3.3. SiS

Results: Next to CO, SiS is the molecule with the most molecular line transitions at our disposal. From the SiS(5–4) up to SiS(20–19), excitation temperatures from 13 to 183 K are covered, and one can trace the envelope abundance spatial variations between 40 and 6000 R_* . The lower lying transitions (SiS(5–4) and (6–4)) probe material at larger radial distances from the star; the SiS(19–18) and (20–19) line intensities are sensitive to the abundance in the inner wind region. Modeling the strength of the low and high-excitation lines gives evidence of a depletion of SiS: the abundance at 40 R_* is estimated to be $\sim 5.5 \times 10^{-6}$ and decreases to $\sim 4 \times 10^{-9}$ at 120 R_* . This is also evidenced by the extra sub-structure in the high signal-to-noise high-resolution

line profiles of the higher excitation lines observed with JCMT and IRAM, where the small peak traces a high abundance component at low velocity close to the star and the broader plateau the lower abundance component further away in the envelope. SiS can be depleted due to the adsorption of SiS molecules onto dust grains, before being photodissociated much farther away. Using ISI 11 μm interferometric data, Hale et al. (1997) detected dust excess, with a first intensity peak around $0.1''$, going out up to at least $0.7''$ (or $2.8 \times 10^{15} \text{ cm} \approx 180 R_*$) around IK Tau. SiS condensation onto dust species has been postulated already (e.g. Bieging & Tafalla 1993), but not all atomic Si or molecular SiS should condense onto dust species (e.g. Dominik et al. 1993). The different rotational lines give us the potential to constrain the compact, pre-condensation, SiS fractional abundance component quite well, but the uncertainty on the extended post-condensation component is higher.

Comparison to theoretical predictions: The abundance at 40 R_* is higher than the theoretical value predicted in the inner wind envelope by Duari et al. (1999) and Cherchneff (2006). This may either indicate that the destruction reaction which oc-

Table 7. Mass-loss rate values derived from ^{12}CO rotational line transitions for IK Tau. The first and second columns list the distance and $[\text{CO}/\text{H}_2]$ value used in the different studies, the third column gives the derived gas mass-loss rate, the fourth column contains the mass-loss rate scaled to our adopted values for the distance ($D = 265$ pc) and CO-abundance ($[\text{CO}/\text{H}_2] = 2 \times 10^{-4}$) using the scaling laws deduced by De Beck et al. (2010), the fifth column lists the rotational line transitions used, and last column gives the reference.

D [pc]	$[\text{CO}/\text{H}_2]$	\dot{M} [M_{\odot}/yr]	\dot{M} (scaled) [M_{\odot}/yr]	Lines	Reference
350	2×10^{-4}	1.0×10^{-5}	6.7×10^{-6}	$^{12}\text{CO}(1-0)$	Bujarrabal et al. (1989)
270	5×10^{-4}	4.0×10^{-6}	6.8×10^{-6}	$^{12}\text{CO}(1-0)$	Sopka et al. (1989)
260	5×10^{-4}	4.4×10^{-6}	7.9×10^{-6}	$^{12}\text{CO}(1-0)$	Loup et al. (1993)
260	5×10^{-4}	3.8×10^{-6}	6.8×10^{-6}	$^{12}\text{CO}(1-0)$	Neri et al. (1998)
250	2×10^{-4}	3.0×10^{-5}	3.2×10^{-5}	$^{12}\text{CO}(1-0) \rightarrow (4-3)$	González Delgado et al. (2003)
250	3×10^{-4}	4.7×10^{-6}	6.5×10^{-6}	$^{12}\text{CO}(1-0) \rightarrow (3-2)$	Teyssier et al. (2006)
300	2×10^{-4}	1.0×10^{-5}	7.7×10^{-6}	$^{12}\text{CO}(1-0) \rightarrow (4-3)$	Ramstedt et al. (2008)
265	2×10^{-4}	9.0×10^{-6}	9.0×10^{-6}	$^{12}\text{CO}(1-0) \rightarrow (7-6)$	this study

curs at larger radii in the inner O-rich envelope via (Cherchneff 2006)



is not as efficient, or that an extra formation route is not yet taken into account in the theoretical modeling. In general, the uncertainties on chemical reaction rates involving sulfur are still very high (I. Cherchneff, *priv. comm.*). The high abundance around $40 R_*$ is in accordance with the observational suggestion by Decin et al. (2008b) that SiS forms close to the star, whatever the C/O ratio of the target.

Comparison to observational studies: Similar results concerning the depletion of SiS in the intermediate wind region are obtained by Schöier et al. (2007a). From the simplified analyses assuming optically thin emission thermalized at one excitation temperature (see Table 6) it is not possible to derive this kind of abundance depletion pattern.

4.3.4. SiO

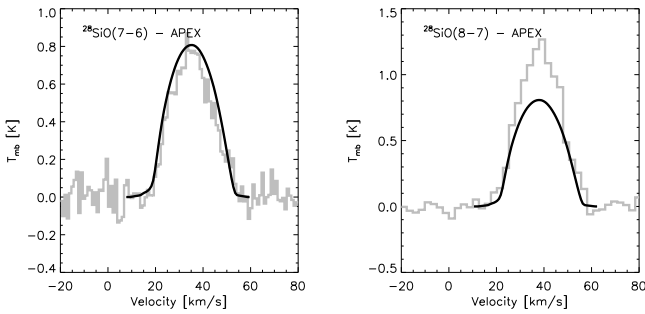


Figure 9. ^{28}SiO observed spectral lines (gray) are compared to the spectral line predictions based on the CSE model shown in Fig. 4 and the abundance stratification displayed in Fig. 5.

Results: For the ^{28}SiO isotopolog, 5 transitions were observed, with excitation energies ranging between 6 and 75 K. The line

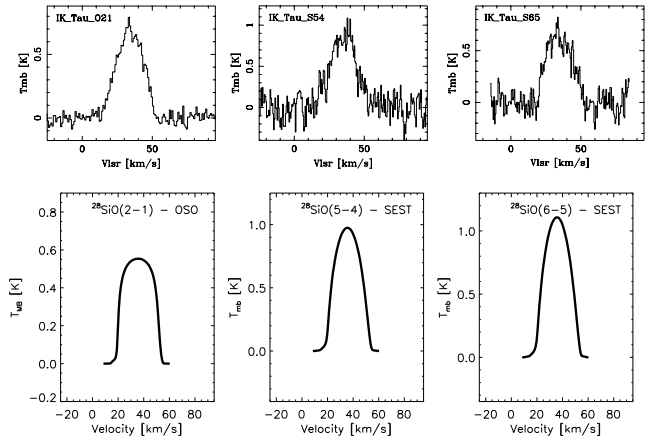


Figure 10. *Upper panel:* ^{28}SiO spectra of IK Tau from González Delgado et al. (2003). *Lower panel:* ^{28}SiO spectral line predictions based on the CSE model shown in Fig. 4 and the abundance stratification displayed in Fig. 5.

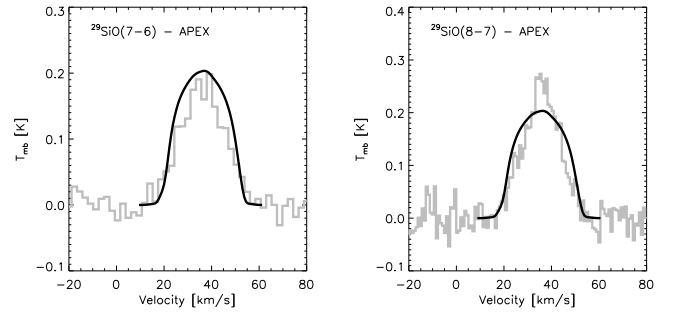


Figure 11. ^{29}SiO observed spectral lines (gray) are compared to the spectral line predictions based on the CSE model shown in Fig. 4 and the abundance stratification displayed in Fig. 5.

strengths and profile shapes of all ^{28}SiO , ^{29}SiO , and ^{30}SiO lines are well predicted, except for the $^{28}\text{SiO}(6-5)$ line as observed with the SEST by González Delgado et al. (2003) (see Fig. 10). Since the strength of both the $^{28}\text{SiO}(5-4)$ and $^{28}\text{SiO}(7-6)$ are well reproduced, and both of these lines share the line formation

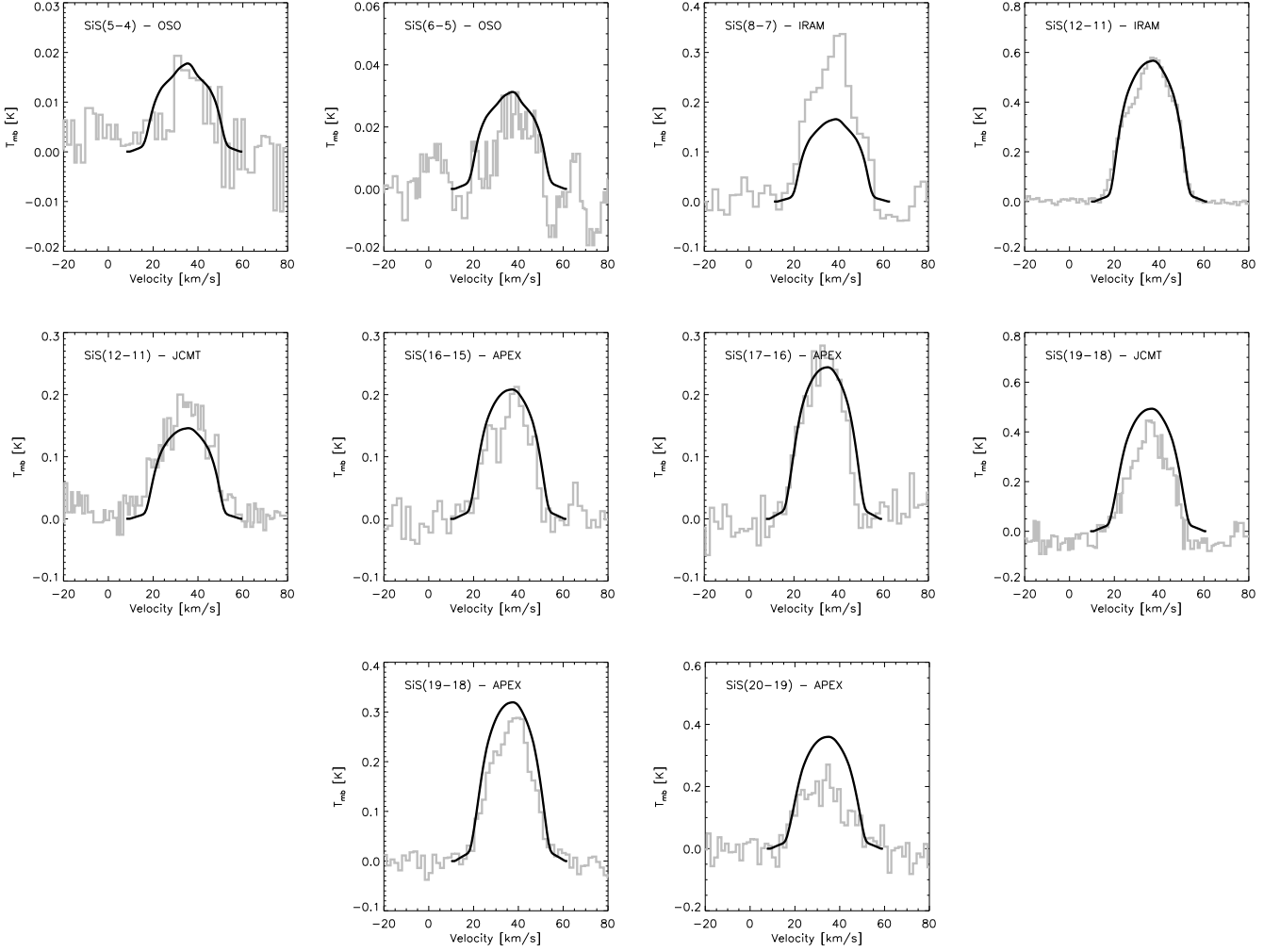


Figure 8. SiS observed spectral lines (gray) are compared to the spectral line predictions based on the CSE model shown in Fig. 4 and the abundance stratification displayed in Fig. 5.

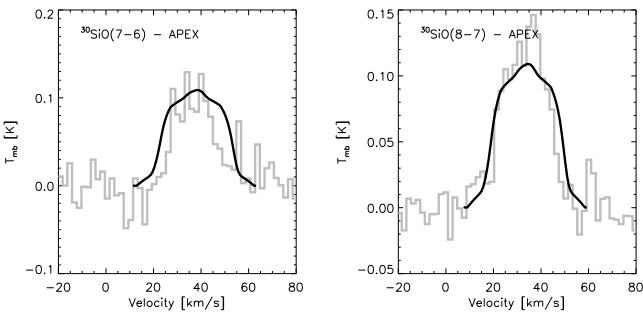


Figure 12. ^{30}SiO observed spectral lines (gray) are compared to the spectral line predictions based on the CSE model shown in Fig. 4 and the abundance stratification displayed in Fig. 5.

region with the $^{28}\text{SiO}(6-5)$ transition, an absolute calibration uncertainty can be the cause of this discrepancy, but time variability of the lines should also be considered (see Sect. 5.1).

Although not as pronounced as for SiS, the modeling of the different rotational transitions indicates an abundance decrease

with a factor ~ 40 around $180 R_*$. SiO is a parent molecule and a strong candidate to be depleted in the wind of O-rich envelopes: at larger radii in the inner envelope, OH alters the SiO abundance via (Cherchneff 2006)



SiO_2 may condense as silica. It may also participate in the formation of amorphous or crystalline silicates.

The derived isotopic ratios in the envelope are $[\text{^{28}SiO}/\text{^{29}SiO}] \sim 27$ and $[\text{^{28}SiO}/\text{^{30}SiO}] = 80$, $[\text{^{29}SiO}/\text{^{30}SiO}] = 3$. They are discussed in Sect. 5.2.

Comparison to theoretical predictions: The SiO abundance at the inner dust condensation radius is slightly below the theoretical predictions of Duari et al. (1999) and Cherchneff (2006), which is very reasonable taking the assumptions of both the theoretical chemical kinetic calculations and our modeling into account. It possibly points toward the condensation of SiO onto dust grains in the intermediate wind zone, before $70 R_*$, a region where our observed lines are not very sensitive to the exact abundance distribution. The observational study by Decin et al. (2008b) indicates that SiO is formed close to the star, in sup-

port of the theoretical predictions by Duari et al. (1999) and Cherchneff (2006). In the outer envelope, SiO is very stable and only photodissociated around a few thousand stellar radii (Willacy & Millar 1997).

Comparison to observational studies: Lucas et al. (1992) mapped the $^{28}\text{SiO}(2-1)v = 0$ flux distribution, showing that it has a circular geometry. The half-peak intensity radius has a diameter of $2.2 \pm 0.1''$ (or a radius of 4.35×10^{15} cm at 265 pc, in our model being $190 R_*$). The SiO(2-1) emission regions indicate that the final expansion velocity is not yet reached in the SiO emission region, suggesting that grain formation must still take place as far as 10^{16} cm from the star. This supports our results on the velocity structure based on the study of the HCN line profiles (Sect. 4.1).

Compared to other observational studies, the deduced abundance around $70 R_*$ is quite high, while the outer wind abundance agrees with the result by González Delgado et al. (2003).

4.3.5. CS

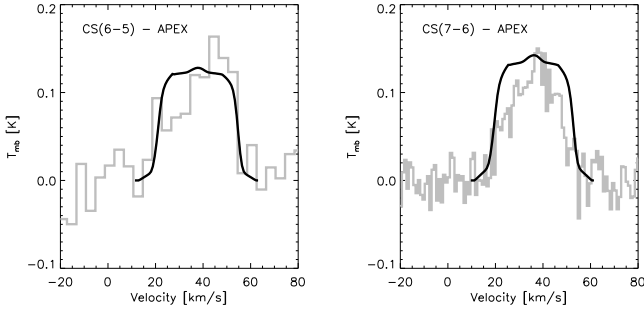


Figure 13. CS observed spectral lines (gray) are compared to the spectral line predictions based on the CSE model shown in Fig. 4 and the abundance stratification displayed in Fig. 5.

Results: For CS, we only have two lines at our disposal, the (6-5) and (7-6) rotational transitions, both with a low S/N-ratio. The fractional abundance at $300 R_*$ is estimated to be $\sim 4 \times 10^{-8}$.

Comparison to theoretical predictions: The derived abundance of $\sim 4 \times 10^{-8}$ is much higher than the TE-abundance of 2.5×10^{-11} for an oxygen-rich star. Cherchneff (2006) predicts CS to be a parent molecule, with a non-TE abundance for TX Cam around 1.8×10^{-5} at $2 R_*$ and around 2×10^{-6} at $5 R_*$ away in the envelope, while Duari et al. (1999) predicts a value of 2.75×10^{-7} at $2.2 R_*$. In their theoretical modeling of the carbon-rich AGB-star IRC+10216 Millar et al. (2001) also argue for the need of CS as a parent species to account for the vibrationally excited CS lines detected in IRC+10216.

As in the case of HCN (Sect. 4.3.2), our derived abundances are a factor ~ 50 lower compared to the predictions of Cherchneff (2006) and a factor ~ 8 lower compared to Duari et al. (1999). The dominant formation pathways of both CS and HCN occur in the fast chemistry zone of the gas parcel excursion involving CN. Knowing that this zone is very difficult

to model (see Sect. 4.3.2) and that the sulfur reaction rates are not well known (see Sect. 4.3.3), this difference is not so cumbersome. However, as suggested for HCN, it may also be the case that CS or the radical CN are involved in dust formation, altering its abundance in the intermediate wind region. The low-resolution of the two observed CS lines do not provide enough information to firmly prove this. In the outer envelope, CS is first formed from H_2S . Somewhat farther away, the reaction of atomic carbon with SO and HS forms CS, before it is photodissociated by UV radiation (Willacy & Millar 1997).

Comparison to observational studies: While our deduced CS fractional abundance agrees with the values derived by Bujarrabal et al. (1994) and Kim et al. (2010), the observational result by Lindqvist et al. (1988) is higher by a factor ~ 4 .

4.3.6. CN

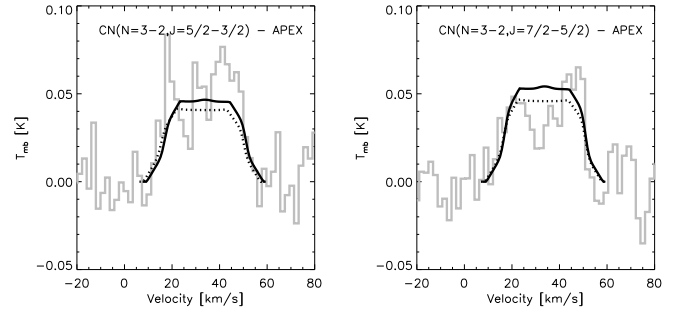


Figure 14. CN observed spectral lines (gray) are compared to the spectral line predictions based on the CSE model shown in Fig. 4 and the abundance stratification displayed in Fig. 5. The dashed line predictions corresponds to the ‘alternative solution’ as shown in Fig. 5.

Results: The CN lines display a peculiar profile, probably related to the hyperfine structure of the molecule. Although the signal-to-noise of the individual components is low, Kim et al. (2010) noted already that the strength of the different peaks are not in agreement with the optical thin ratio of the different hyperfine structure components and hint to hyperfine anomalies as already reported by Bachiller et al. (1997). Simulations with the GASTRoNoOM-code taking all the hyperfine components into account confirm this result. We therefore opt to simulate both CN lines using the strongest component only. I.e., for the $N = 3 - 2, J = 5/2 - 3/2$ line we will use the $F = 7/2 - 5/2$ component at 340031.5494 MHz, for the $N = 3 - 2, J = 7/2 - 5/2$ line the $F = 9/2 - 7/2$ component at 340248.5440 MHz is used.

Due to low signal-to-noise ratio of the lines and the problems with the different hyperfine components, the derived abundance fractions are loosely constrained. To illustrate this, two model predictions are shown in Fig. 14. For one model, the inner abundance ratio is taken to be 3×10^{-8} and from $1000 R_*$ onward, the abundance stratification follows the predictions by Willacy & Millar (1997) (dashed line in Fig. 5). For the other model, the inner abundance ratio, f_1 , is lowered to 1×10^{-10} yielding a peak fractional abundance around $2000 R_*$ of $\sim 2.5 \times$

10^{-6} , being a factor ~ 8 higher than the peak fractional abundance derived by Willacy & Millar (1997) (see dotted line in Fig. 5).

Comparison to theoretical predictions: The predicted inner wind abundance fractions give higher preference to the second model described in previous paragraph: Duari et al. (1999) predicts a fractional abundance of CN around 2.4×10^{-10} at $2.2 R_*$ for IK Tau, while Cherchneff (2006) gives a value of 3×10^{-10} at $5 R_*$ for TX Cam. Further out in the wind, CN is produced by neutral-neutral reactions and the photodissociation of HCN, yielding peak fractional abundances around 3×10^{-7} (Willacy & Millar 1997).

If HCN is indeed photodissociated around 400 to $500 R_*$ (see Sect. 4.3.2), the peak fractional abundance of CN is not expected to occur around $2000 R_*$ (see the model predictions by Willacy & Millar 1997, in Fig. 5), but slightly beyond $500 R_*$ since the photodissociation of HCN is the main formation route to CN in the outer envelope. Shifting the CN peak fractional abundance in the second model to $500 R_*$ with an abundance value of 1.5×10^{-7} also yields a good fit to the (noisy) data.

Comparison to observational studies: This is the first time that the non-LTE CN fractional abundance for IK Tau has been derived, although the uncertainty on the derived abundance is large.

4.3.7. SO

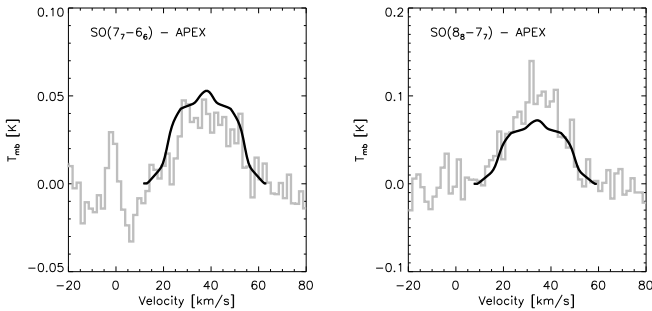


Figure 15. SO observed spectral lines (gray) are compared to the spectral line predictions based on the CSE model shown in Fig. 4 and the abundance stratification displayed in Fig. 5.

Results: As in case of CN (Sect. 4.3.6) the noisy profiles prevent a good determination of the abundance stratification. A fractional abundance of $\sim 2 \times 10^{-7}$ is derived around $200 R_*$.

Comparison to theoretical predictions: An abundance stratification compatible with both the inner wind predictions of Cherchneff (2006) and the outer wind model of Willacy & Millar (1997) can be derived yielding a good representation of both SO lines observed with APEX. Willacy & Millar (1997) assumed no SO injection from the inner wind at large radii, but in-situ formation processes only. Assuming that SO is indeed injected to larger radii can in-

crease the predicted peak fractional abundance computed by Willacy & Millar (1997) which was somewhat too low compared to the observed value listed in their Table 6.

Comparison to observational studies: For the first time, the SO abundance fraction is derived using a non-LTE radiative transfer analysis, although the low S/N prevents an accurate abundance determination. The result agrees with the LTE analysis by Kim et al. (2010), but is a factor of a few lower than Omont et al. (1993) and Bujarrabal et al. (1994).

4.3.8. SO₂

As for SO₂ the main formation channel in both the inner and outer wind region is



In the outer wind, SO₂ rapidly photodissociates back to SO (Willacy & Millar 1997). The inner wind predictions for TX Cam only yield an abundance of $\sim 1.3 \times 10^{-12}$, but the detection of SO₂ at $7.3 \mu\text{m}$ in several O-rich giants (Yamamura et al. 1999) would imply a formation site close to the star and an abundance in the range $10^{-8} - 10^{-7}$, slightly below the SO values. Cherchneff (2006) argues that a limited number of reactions in the involved SO₂ formation scheme and the lack of measured reaction rates may explain this discrepancy.

Results: The availability of 10 different transitions gives some hope that we can shed light on the discussion about the inner wind fractional abundance. However, it turns out that we are unable to fit the high-excitation SO₂(17_{1,17} – 16_{0,16}) and SO₂(13_{2,12} – 12_{1,11}) lines observed with APEX (see below). The high-excitation SO₂(14_{4,10} – 14_{3,11}) and SO₂(14_{3,11} – 14_{2,12}) can be predicted quite well. These two lines are narrower than the other SO₂ lines in the sample, indicating that their full formation region is in the inner wind region where the wind has not yet reached its full expansion velocity.

Extensive modeling efforts were done to predict the high-excitation SO₂ observed with APEX. While the high-excitation lines involving the $J = 14 - 14$ levels are reasonably well predicted with the models proposed above, the $J = 13 - 12$ and $J = 17 - 16$ are far too weak. In a study of SO₂ in star forming regions, van der Tak et al. (2003) encountered an analogous problem, which they solved by introducing a high temperature, high-abundance component. The increase in abundance could be a factor of 100–1000. Introducing an unrealistic compact, very high-abundance component with $f_1 > 1 \times 10^{-4}$ up to $200 R_*$ reproduces the APEX $J = 13 - 12$ and $J = 17 - 16$ within a factor 2, but the $J = 14 - 14$ lines, involving similar excitation levels, is a factor ~ 15 too strong. A possible cause of the discrepancy could be a misidentification of the observed lines. However, different line data bases always point towards an identification as SO₂ transitions. But also the collision rates from the LAMDA database may be problematic. In the LAMDA database, Schöier et al. (2005) have extrapolated the collisional rates as computed by Green (1995). Green (1995) computed the collisional rates for temperatures in the range from 25 to 125 K including energy levels up to 62 cm^{-1} ; Schöier et al. (2005) extrapolated this set of collisional rates to include energy levels up to 250 cm^{-1} and for a range of temperatures from 10 to 375 K.

Neglecting the SO₂(17_{1,17}–16_{0,16}) and SO₂(13_{2,12}–12_{1,11}) lines, the strength of the other eight SO₂ lines can only be explained using a high inner abundance ratio of 1×10^{-6} , clearly

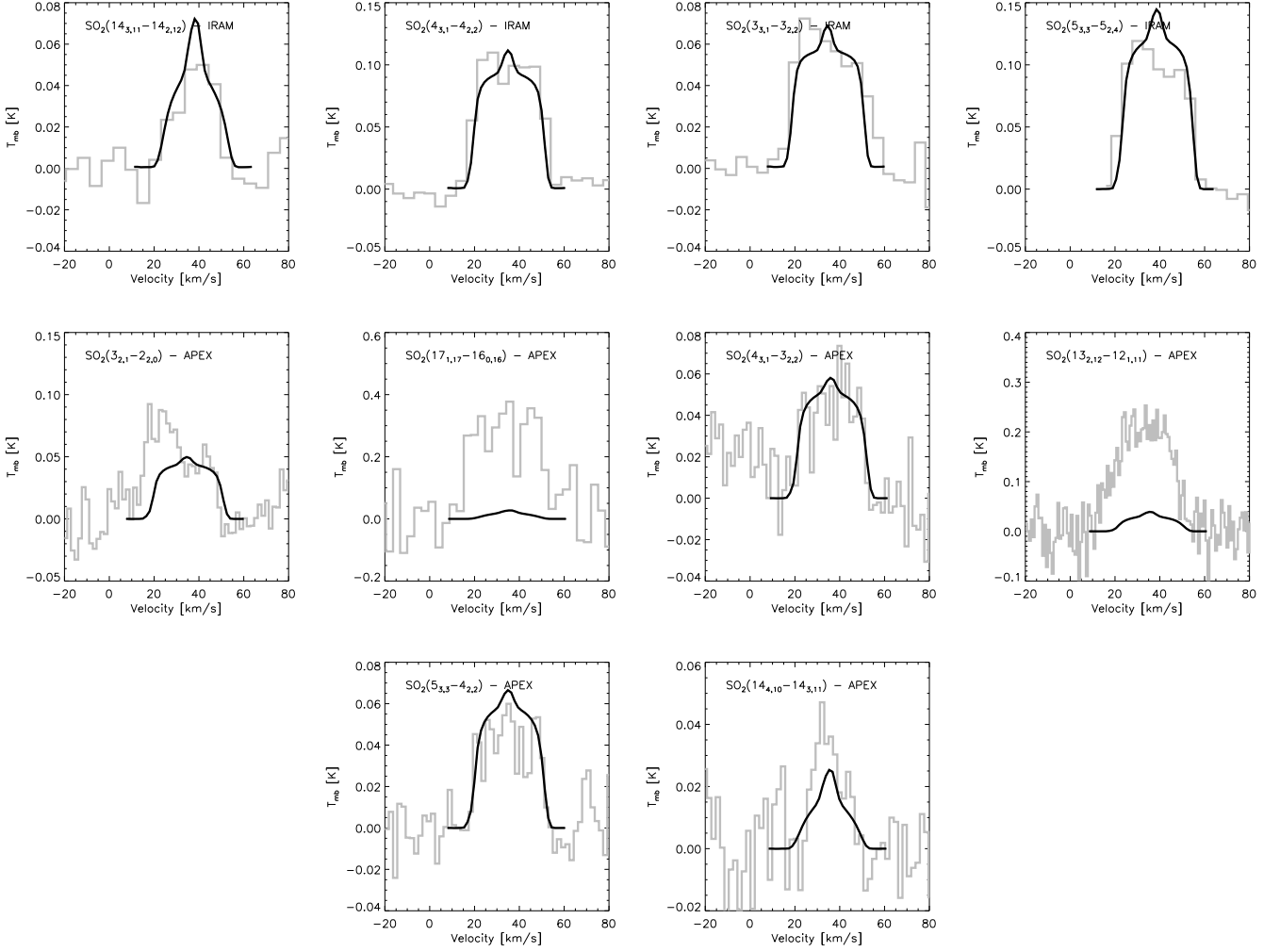


Figure 16. SO_2 observed spectral lines (gray) are compared to the spectral line predictions based on the CSE model shown in Fig. 4 and the abundance stratification displayed in Fig. 5.

pointing toward an inner wind formation region (in accordance with Yamamura et al. 1999).

Comparison to observational studies: As for SO , the SO_2 fractional abundance is derived for the first time using a full non-LTE radiative transfer analysis. The derived abundance value is somewhat lower than the results from classical studies assuming optically thin emission and one excitation temperature, although we have to state clearly that the SO_2 modeling still poses many problems.

5. Discussion

The derived fractional abundances are already discussed in Sect. 4.3. In this section, we focus on the possible time variability of the emission lines and on the derived SiO isotopic ratios. In the last part, H_2O line profile predictions for the Herschel/HIFI mission are performed.

5.1. Time variability

The observed molecular emission lines could be time variable. Unfortunately, no dedicated study has yet been performed to study the time variability of the molecular lines in IK Tau. Carlström et al. (1990) reported on a monitoring programme of the $\text{SiS}(J=4-3, 5-4, \text{ and } 6-5)$ emission from the Mira-type carbon-rich AGB star IRC +10216. It was found that the circumstellar $J=5-4$ and $J=6-5$ line emission toward IRC +10216 varies both in line intensity and in line shape. A clear correlation between the variations and the infrared flux (as measured using the K -band magnitude) is found for the $J=5-4$ and $J=6-5$ lines (Bieging & Tafalla 1993), but not for the $J=4-3$ line. This indicates that, at least, the population of a few levels vary in phase with the stellar flux. A change in the pumping mechanism of the infrared vibrationally excited levels of a molecule will modify the excitation in the ground vibrational state. A change in dust emission may also alter the excitation of a molecule, since dust emission has the potential of affecting the level populations in the ground vibrational state, in particular through pumping via excited vibrational states.

Cernicharo et al. (2000) have looked for time-related intensity variations in a line survey at 2 mm of IRC+10216. Among

the 2-mm lines, the most likely lines to be affected are: (i) CS, HC₃N, SiO and SiS, four species whose IR lines are known to be optically thick, as well as (ii) the vibrationally excited lines of C₄H and HCN. During the 10-year long run, these lines were observed at several occasions. The ground-state mm lines were found to have stable shapes and intensities (within 20% which is consistent with the calibration uncertainty). Only the strong HCN, $\nu_2 = 1$, $J = 2 - 1$ line, which is known to be masering, showed a factor of 2 intensity variation with time.

Currently the effect of time variability on circumstellar line emission is unknown for AGB stars in general.

5.2. SiO isotopic ratios

The SiO abundance isotopic ratios derived for IK Tau are $^{28}\text{SiO}/^{29}\text{SiO} = 27$, $^{28}\text{SiO}/^{30}\text{SiO} = 80$, and $^{29}\text{SiO}/^{30}\text{SiO} = 3$, with an uncertainty of a factor of ~ 2 due to the low signal-to-noise ratio of the ^{29}SiO and ^{30}SiO lines. The $^{29}\text{SiO}/^{30}\text{SiO}$ is similar to the simple ratio of integrated intensities corrected for a difference in transition strength and beam filling factor (the combined effect is a frequency factor of ν^{-2}), but the $^{28}\text{SiO}/^{29}\text{SiO}$ and $^{28}\text{SiO}/^{30}\text{SiO}$ ratios are a factor ~ 7 and ~ 10 larger, respectively, due to neglect of optical depth effects of the ^{28}SiO lines in case the simplified intensity ratio is used. Compared to the solar isotopic ratios of $(^{28}\text{SiO}/^{29}\text{SiO})_{\odot} = 19.6$, $(^{28}\text{SiO}/^{30}\text{SiO})_{\odot} = 29.8$ and $(^{29}\text{SiO}/^{30}\text{SiO})_{\odot} = 1.52$, IK Tau is underabundant in neutron-rich isotopologs or overabundant in ^{28}Si .

Due to the weakness of the ^{29}SiO and ^{30}SiO lines, only few results on the silicon isotopic ratios in the circumstellar envelopes around AGB stars are reported in literature. By fitting the SiO maser emissivity Jiang et al. (2003) estimated the $^{28}\text{SiO}/^{29}\text{SiO}$ isotopic ratio in two oxygen-rich Miras, R Cas and NV Aur, as being 29 and 32, respectively. Ukita & Kaifu (1988) measured the relative intensities of the $^{29}\text{SiO}/^{30}\text{SiO}$ lines ($J = 2 - 1, v = 0$), being 2.4 for the S-type Mira χ Cyg (with C/O ratio slightly lower than 1), 1.5 for IK Tau, and 2.9 for the oxygen-rich Mira V1111 Oph. For the carbon-rich AGB star IRC+ 10216, Cernicharo et al. (2000) and He et al. (2008) derived respectively $^{28}\text{SiO}/^{29}\text{SiO} = 15.4 \pm 1.1$ (17.2 ± 1.1) and $^{28}\text{SiO}/^{30}\text{SiO} = 20.3 \pm 2.0$ (24.7 ± 1.8) and $^{29}\text{SiO}/^{30}\text{SiO} = 1.45 \pm 0.13$ (1.46 ± 0.11) from the ratios of integrated line intensities, being close to the solar values. The results on IRC+10216 are, however, lower limits, since no correction for opacity effects has been done.

Lambert et al. (1987) analysed high-resolution spectra of the SiO first overtone band around $4 \mu\text{m}$. They obtained estimates of the atmospheric $^{28}\text{SiO}/^{29}\text{SiO}$ abundance ratios for four red giants. For the M-type β Peg and the S-type star HR 1105, the $^{28}\text{SiO}/^{29}\text{SiO}$ ratio is close to the solar ratio. ^{29}SiO appears to be underabundant in the MS star σ^1 Ori ($^{28}\text{SiO}/^{29}\text{SiO} = 40$) and the M-type star 10 Dra ($^{28}\text{SiO}/^{29}\text{SiO} \sim 53$). The ^{30}SiO isotope appears to be underabundant by a factor of ~ 2 in all four red giants.

Tsuji et al. (1994) reported on high spectral resolution observations of the $4 \mu\text{m}$ SiO first overtone band in six late-type M giants and two M supergiants. The atmospheric $^{28}\text{Si}/^{29}\text{Si}$ and $^{28}\text{Si}/^{30}\text{Si}$ and $^{29}\text{Si}/^{30}\text{Si}$ ratios in the M giants are always slightly lower than the terrestrial values, i.e. more neutron-rich nuclei tend to be more abundant. This is opposite to the results of Lambert et al. (1987), and assuming that the isotopic ratios are not modified in the circumstellar envelope, the result of Tsuji et al. (1994) is also in contrast to the circumstellar isotopic ratios of M-type giants listed above.

The silicon isotopic ratios are not obviously correlated with other stellar properties. In the literature, it is conventional to express the silicon (and other element) isotope ratios in parts per thousand deviation from the solar silicon isotope ratio:

$$\delta_{\odot}(^{29}\text{Si}) \equiv \delta_{\odot} \left(\frac{^{29}\text{Si}}{^{28}\text{Si}} \right) \equiv 1000 \left[\left(\frac{^{29}\text{Si}}{^{28}\text{Si}} \right) / \left(\frac{^{29}\text{Si}}{^{28}\text{Si}} \right)_{\odot} - 1 \right],$$

$$\delta_{\odot}(^{30}\text{Si}) \equiv \delta_{\odot} \left(\frac{^{30}\text{Si}}{^{28}\text{Si}} \right) \equiv 1000 \left[\left(\frac{^{30}\text{Si}}{^{28}\text{Si}} \right) / \left(\frac{^{30}\text{Si}}{^{28}\text{Si}} \right)_{\odot} - 1 \right], \quad (8)$$

$$(9)$$

yielding values for IK Tau of -274 and -627 , respectively. These values reflect both the initial isotopic composition of the star and possible effects due to nucleosynthesis.

For an AGB star, the initial Si isotopic composition in the envelope is altered by slow neutron capture reactions (*s*-process) in the He intershell and subsequent third dredge-up (TDU) events, increasing the ^{29}Si and ^{30}Si abundance fractions. A low-metallicity star is expected to have initial $^{29}\text{Si}/^{28}\text{Si}$ and $^{30}\text{Si}/^{28}\text{Si}$ ratios that are smaller than the solar ratios. The inferred isotopic shifts of the Si isotopes are smaller for an O-rich than for a C-rich AGB star since a C-rich star goes through more dredge-up events increasing the ^{12}C and *s*-processed material (Zinner et al. 2006; Vollmer et al. 2008). Using two different stellar evolution codes, Zinner et al. (2006) studied the change in silicon isotopic ratios in AGB stars: the shift in Si isotopic ratios and the increase of the $^{12}\text{C}/^{13}\text{C}$ in the envelope during third dredge-up are higher for higher stellar mass, lower metallicity, and lower mass-loss rate, but their predicted silicon isotopic shifts are always much higher than the observational values derived for IK Tau. The minimum values plotted in their Fig. 6 correspond to the value $\delta_{\odot}(^{29}\text{Si})$ and $\delta_{\odot}(^{30}\text{Si})$ at C/O=1, and are larger than -200 . They find that no noticeable changes in the Si isotopes occur when the star is still O-rich. Consequently, the isotopic anomalies in silicon found for several M-type giants probably reflect those of the interstellar medium out of which stars were formed.

For the solar system material, the silicon isotopic ratios are thought to be understood by a mixture of the nuclear products by types I and II supernovae (Tsuji et al. 1994). The predicted silicon isotopic ratios by type II supernovae are around $^{28}\text{Si}/^{29}\text{Si} \sim 15$ and $^{28}\text{Si}/^{30}\text{Si} \sim 35$ according to Hoppe et al. (2009), while Hashimoto et al. (1989) arrive at lower values being 8.9 and 12.6 respectively. Type I supernovae produce mostly ^{28}Si with little ^{29}Si and ^{30}Si (Thielemann et al. 1986). Non-terrestrial silicon isotopic ratios can then be reasonably explained in the same way as for the solar system but by assuming a different contribution of types I and II supernovae.

The silicon isotopic shifts reported here for IK Tau are much lower than values deduced from presolar silicate grains (Vollmer et al. 2008; Mostefaoui & Hoppe 2004), of which the origin spans the range from red giant branch (RGB) and AGB stars up to supernovae. Looking to silicon isotopic ratios derived from presolar SiC grains (Fig. 2 in Zinner et al. 2006), the silicon isotope ratios of IK Tau correspond to the X-grains, which are thought to originate in Type II supernovae (however major discrepancies between model predictions and observed isotopic ratios still exist; Nittler et al. 1995). The $^{12}\text{C}/^{13}\text{C}$ ratio inferred for IK Tau ($=14$) is at the lower limit of the values derived for X-type grains (see Fig. 1 in Zinner et al. 2006).

Hence, if the atmospheric (and circumstellar) silicon isotopic ratio is indeed not changed due to nucleosynthesis and subsequent dredge-ups, the above arguments seem to suggest that the

interstellar medium out of which IK Tau was born has a mixture analogous to X-type grains of which supernovae type II are thought to be the main contributors. The measurement of other isotopic ratios can shed new light on this discussion.

5.3. H₂O line profile predictions

Line profile predictions are performed for a few water lines which will be observed by Herschel/HIFI in the framework of the Guaranteed Time Key Programme HIFISTARS (P.I. V. Bujarrabal) (see Table 8). This key programme focusses on the observations of CO, H₂O and HCN lines in a well-selected sample of evolved stars in order to gain deeper insight into the structure, thermodynamics, kinematics and chemistry of CSEs and into the mass-loss history of evolved stars. The inner wind abundance fraction is assumed to be $[H_2O/H_2]=3.5 \times 10^{-4}$ (Cherchneff 2006). The photodissociation radius is taken from the modeling of Willacy & Millar (1997), being around $1600 R_*$. Using the analytical formula from Groenewegen (1994) deduced from the results of Netzer & Knapp (1987), a photodissociation radius of 2.8×10^{16} cm or $1870 R_*$ would be obtained. As standard set-up, the Barber H₂O line list (see Appendix A) is used, including 45 levels in both the ground state and first excited vibrational state (the bending mode $\nu_2 = 1$ at $6.3 \mu\text{m}$).

Table 8. Line frequencies, upper energy levels and Einstein A-coefficients for the ortho-H₂O lines which will be observed with Herschel/HIFI.

Vibrational state	Transition	Frequency [GHz]	E_{upper} [cm^{-1}]	A [s^{-1}]
$v = 0$	$1_{1,0} - 1_{0,1}$	556.933	42.371	3.497×10^{-3}
$v = 0$	$5_{3,2} - 4_{4,1}$	620.882	50.880	1.106×10^{-4}
$v = 0$	$3_{1,2} - 3_{0,3}$	1097.488	173.365	1.664×10^{-2}
$v = 0$	$3_{1,2} - 2_{2,1}$	1153.219	173.365	2.693×10^{-3}
$v = 0$	$6_{3,4} - 5_{4,1}$	1158.391	648.967	1.417×10^{-3}
$v = 0$	$3_{2,1} - 3_{1,2}$	1162.849	212.154	2.307×10^{-2}
$v = 0$	$8_{5,4} - 9_{2,7}$	1595.961	1255.144	2.947×10^{-4}
$v = 0$	$3_{0,3} - 2_{1,2}$	1716.731	136.757	5.109×10^{-2}
$v = 0$	$7_{3,4} - 7_{2,5}$	1797.168	842.355	9.143×10^{-2}
$v = 0$	$5_{3,2} - 5_{2,3}$	1867.562	508.806	8.198×10^{-2}
$v = 1$	$1_{1,0} - 1_{0,1}$	658.081	1618.683	5.575×10^{-3}
$v = 1$	$8_{2,7} - 7_{3,4}$	967.403	2495.278	5.800×10^{-4}
$v = 1$	$2_{1,2} - 1_{0,1}$	1753.922	1677.187	6.335×10^{-2}

Description of the line profiles: Most H₂O lines displayed in Fig. 17 have a parabolic shape, characteristic for optically thick unresolved emission. A few lines suffer from self-absorption in the blue wing (e.g., the $8_{5,4} - 9_{2,7}$ line in the ground-state). Particularly for lines where the optical depths at the line centre can be up to ~ 100 , effective self-absorption on the blue-shifted side can be seen (e.g., the $1_{1,0} - 1_{0,1}$ and $3_{0,3} - 2_{1,2}$ lines in the ground-state). Lines in the first vibrational state allow one to trace the wind acceleration zone. These lines are considerably narrower than $2 v_\infty$ (e.g., the $8_{2,7} - 7_{3,4}$ line in the $\nu_2 = 1$ -state).

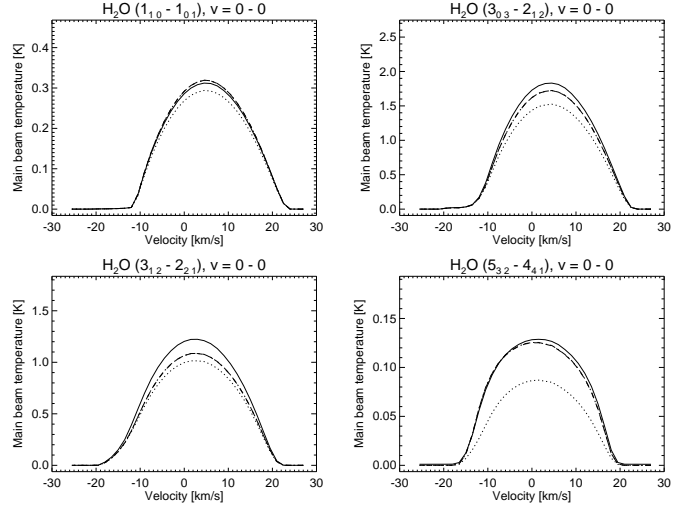


Figure 18. Comparison between H₂O line profile predictions using (1) the Barber line list, including the ground-state and $\nu_2 = 1$ -state (full line, see also Fig. 17), (2) the LAMDA line list, including only the ground-state (dotted line), (3) the LAMDA line list, including the ground-state and $\nu_2 = 1$ -state (dashed line), and (4) the LAMDA line list, including the ground-state, the $\nu_2 = 1$ -state and $\nu_3 = 1$ -state (dash-dotted line). One can barely see the difference between including or omitting the $\nu_3 = 1$ -state in the predictions for IK Tau, the only exception to this is the center of the optically thin $8_{54} - 9_{27}$ line in the ground state.

Comparison to other line lists, including or omitting the ν_2 and ν_3 vibrational state (see Fig. 18): Using the Barber H₂O or the LAMDA linelist yields comparable results for the lines displayed here. Omitting the first vibrational state of the bending mode ($\nu_2 = 1$), yields a decrease in line flux of a few percent up to 60 percent at maximum, depending on the transition. This discrepancy will increase for lower mass-loss rate objects (Maercker et al. 2008). The inclusion of excitation to the first excited vibrational state of the asymmetric stretching mode ($\nu_3 = 1$) yields a change in line flux of 20 % at maximum. This is in agreement with the recent results by González-Alfonso et al. (2007) and Maercker et al. (2009), who found that the inclusion of the $\nu_3 = 1$ -state is particularly important for low mass-loss rate objects. Since the Einstein A-coefficients of the symmetric stretching mode ($\nu_1 = 1$) are an order of magnitude lower than for the asymmetric stretching, this state is not likely to affect the models.

Dependence on parameters: The H₂O line fluxes which will be observed with HIFI are very sensitive to certain (stellar) parameters, and their observations will give us a handle to constrain the circumstellar structure to even higher accuracy. To illustrate this, some simulations are shown in Fig. 19.

- In case the temperature structure is approximated using a power law $T(r) \sim r^{-0.7}$ (dotted line in Fig. 19), a differential change is seen for the predicted line fluxes. Observing a few water lines with different excitation levels will pin down the temperature structure in the CSE.
- A second simulation shows the effect of using a velocity structure which is computed from solving the momentum equation (dashed-dotted line in Fig. 19). Using another velocity law results in another gas number density and slightly

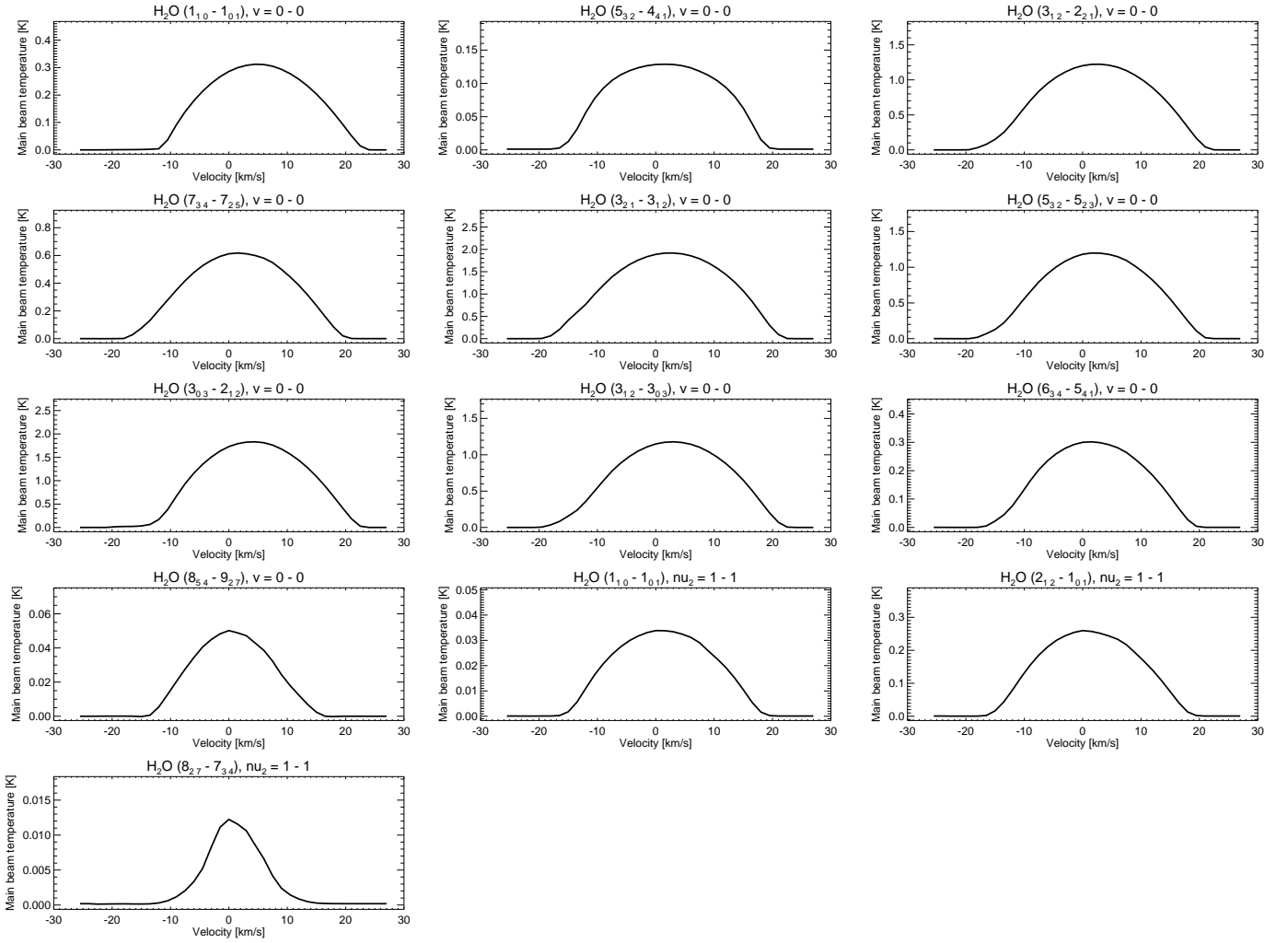


Figure 17. Snapshot of a few ortho- H_2O lines which will be observed with Herschel/HIFI.

different temperature structure. Using the momentum equation, a steeper velocity gradient is obtained (see, e.g., Fig. 3), and the velocity reaches the terminal velocity at shorter distances from the star. This results in slightly broader line profiles and a flux enhancement in the blue wing since that part of the CSE contributing to the line profile at a certain velocity v will be shifted somewhat inward, hence attaining a higher source function.

- Using a blackbody to represent the stellar radiation instead of a high-resolution theoretical spectrum calculated from a MARCS model atmosphere (see Sect. 3.1), only induces a change in the predicted line fluxes smaller than 2% (not shown in Fig. 19). For wavelengths beyond $200\ \mu\text{m}$ the stellar flux is always represented by a blackbody in the GASTRoNOm-calculations (note that the ground-state of ortho-water is at $23.794\ \text{cm}^{-1}$ or around $420\ \mu\text{m}$), the flux difference between the blackbody and the theoretical high-resolution spectrum around the ν_2 bending mode is shown Fig. 20. The reason for this negligible difference is the fact that the stellar radiation field is not important (in this case) for the H_2O excitation. Excluding the stellar radiation field only yields a reduction of the line emission by 2% at maximum.
- The dashed line in Fig. 19 shows the model predictions using the same stellar and envelope parameters as in

Maercker et al. (2008): $T_{\text{eff}} = 2600\ \text{K}$, $R_* = 3.53 \times 10^{13}\ \text{cm}$, $D = 300\ \text{pc}$ and $\dot{M} = 1 \times 10^{-5}\ M_{\odot}/\text{yr}$. This example shows how maser action in the $5_{32} - 4_{41}$ transition at 621 GHz is very sensitive to the structural parameters.

6. Conclusions

In this paper, we have for the first time performed a self-consistent, non-LTE radiative transfer analysis on 11 different molecules and isotopologs (^{12}CO , ^{13}CO , SiS, ^{28}SiO , ^{29}SiO , ^{30}SiO , HCN, CN, CS, SO, SO_2) excited in the circumstellar envelope around the oxygen-rich AGB star IK Tau. In contrast to previous studies, the temperature and velocity structure in the envelope are computed self-consistently, the circumstellar fractional abundances are linked to theoretical outer wind non-chemical equilibrium studies and the full line profiles are used as criteria to deduce the abundance structure. The Gaussian line profiles of HCN and SiO clearly point toward formation partially in the region where the wind has not yet reached its full velocity. Using the HCN line profiles as criterion, we can deduce that the wind acceleration is slower than deduced from classical theories (e.g. Goldreich & Scoville 1976). For a few molecules, a significantly different result is obtained compared to previous, more simplified, studies. SiO and SiS seem to be depleted in the intermediate wind region due to adsorption onto dust

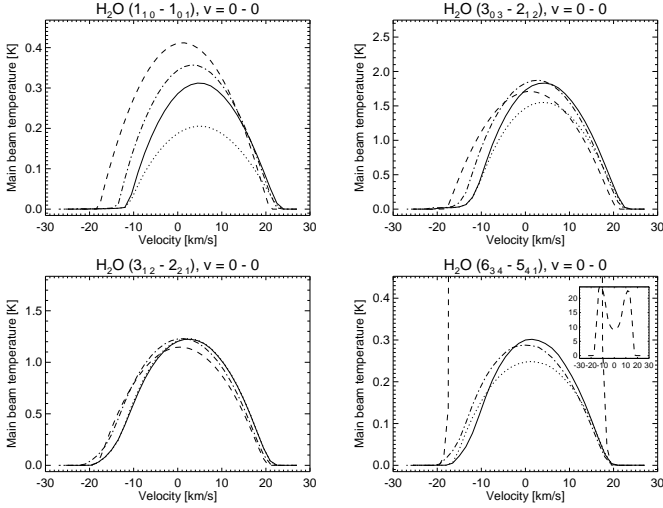


Figure 19. Comparison between H_2O line profile predictions using the Barber line list, including the ground-state and $\nu_2 = 1$ -state (1) full line: predictions using temperature and velocity structure as shown in Fig. 4 (see also Fig. 17), (2) dotted line: assuming a power law temperature structure $T(r) \sim r^{-0.7}$, (3) dashed-dotted line: assuming a velocity structure consistent with the momentum equation (see discussion in Sect. 4.1), (5) dashed line: assuming the same stellar parameters as used by Maercker et al. (2008): $T_{\text{eff}} = 2600$ K, $R_* = 3.53 \times 10^{13}$ cm, $D = 300$ pc and $\dot{M} = 1 \times 10^{-5} M_{\odot}/\text{yr}$. The inset in the lower right panel shows the full maser line profile of the $6_{34} - 5_{41}$ transition using these parameters.

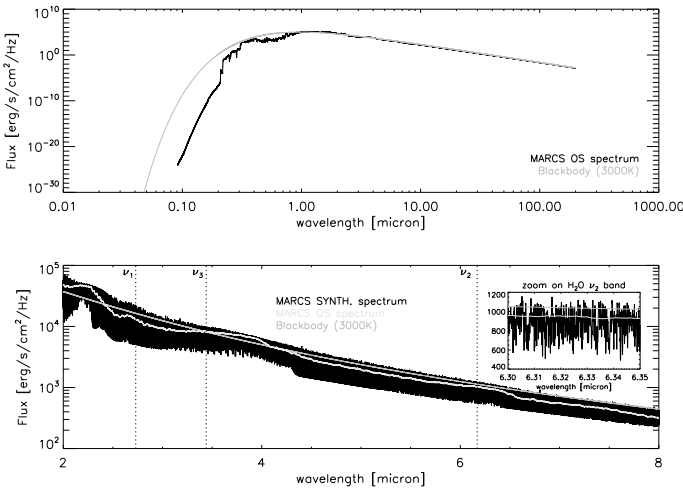


Figure 20. Representation of the stellar radiation field. *Upper panel:* Comparison between a blackbody at 3000 K (gray) and a MARCS flux-sampled spectrum at a stellar temperature of 3000 K and a logarithm of the gravity of 1.5 dex (black). *Lower panel:* Comparison between a blackbody at 3000 K (gray), a MARCS flux-sampled spectrum (light gray) and a high-resolution theoretical spectrum generated from the MARCS model with a resolution of $\Delta\lambda = 0.5\text{\AA}$ in the wavelength region between 2 and $8\ \mu\text{m}$. The bandheads of the different water vibrational modes (the symmetric stretching mode ν_1 , the bending mode ν_2 , and the asymmetric stretching mode ν_3) are indicated by the vertical dotted lines. The inset shows a zoom around $6.3\ \mu\text{m}$ where water absorption determines the spectral appearance.

grains. The HCN and CS intermediate wind abundance around $50\text{--}300 R_*$ is clearly below the inner wind theoretical predictions by Duari et al. (1999) and Cherchneff (2006), which may either indicate a problem in the theoretical shock-induced modeling or possibly that, contrary to what is thought, HCN and CS do participate in the dust formation, maybe via the radical CN through which both molecules are formed. The lack of high signal-to-noise data for CN and SO prevent us from accurately determining the circumstellar abundance stratification. It turned out to be impossible to model all the SO_2 line profiles, particularly a few of the high-excitation lines. This may be due to a misidentification of the lines or to problems with the collisional rates. The SiO isotopic fractions point toward high $^{28}\text{SiO}/^{29}\text{SiO}$ and $^{28}\text{SiO}/^{30}\text{SiO}$ ratios, which are currently not understood in the framework of nucleosynthesis altering the AGB isotopic fractions, but seem to reflect the chemical composition of the interstellar cloud out of which the star is born. Finally, in Sect. 5.3, we present H_2O line profile predictions for a few lines which will be observed with the Herschel/HIFI instrument (launched on May, 14 2009).

Appendix A: Molecular line data

For each of the treated molecules, we briefly describe the molecular line data used in this paper. Quite often, data from the *Leiden Atomic and Molecular Database* (LAMDA) are used (Schöier et al. 2005). When appropriate, transition probabilities are compared to the relevant data in this database.

CO – carbon monoxide. Both for ^{12}CO and ^{13}CO , energy levels, transition frequencies and Einstein A coefficients were taken from Goorvitch & Chackerian (1994). Transitions in the ground and first vibrational state were included up to $J = 40$. The CO- H_2 collisional rate coefficients at kinetic temperatures from 10 to 4000 K are from Larsson et al. (2002). Figure A.1 shows a good match for the transition frequencies (better than 1%). The Einstein A coefficients for the rotational transitions in the ground-state and the vibra-rotational transitions correspond to better than 0.5%, but the Einstein A coefficients for the rotational transitions in the $v = 1$ state may differ by up to a factor 3 for the high-lying rotational transitions, i.e. the ones with the largest J quantum number. For the CO lines of interest to this study, i.e. rotational transitions in the $v = 0$ state with $J_{\text{up}} \leq 7$, the effect on the predicted line fluxes is small: calculating the temperature stratification self-consistently (see Sect. 3.1) using the Einstein A coefficients of the LAMDA-data base, the largest deviation (of 6%) occurs for the $^{12}\text{CO}(1-0)$ line.

SiO – silicon monoxide. The SiO linelist of Langhoff & Bauschlicher (1993) was used to extract the frequencies, energy levels and (vibra-)rotational radiative rates for ^{28}SiO , ^{29}SiO , and ^{30}SiO . Both ground and first vibrational state were included, with rotational quantum number J up to 40. The SiO- H_2 collisional rates in the ground state are taken from the LAMDA-database. For the rotational transitions in the first vibrational state, it is assumed that the collisional rates are equal to the ones in the ground state. The vibra-rotational collisional rates are assumed to be zero.

The LAMDA database only lists the frequencies and transition probabilities for the first 40 levels in the ground state. Comparison with the line list of Langhoff & Bauschlicher (1993) shows that both databases nicely agree for the rotational transitions in the ground state (see Fig. A.2).

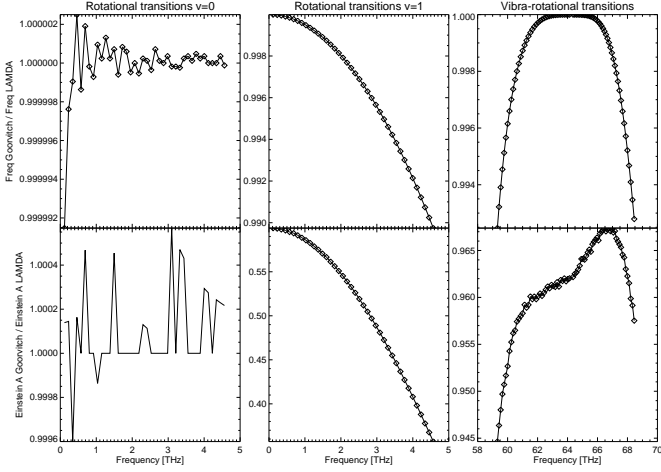


Figure A.1. Comparison between the transition frequencies and Einstein A coefficients of CO as listed in the LAMDA database and as computed by Goorvitch & Chackerian (1994).

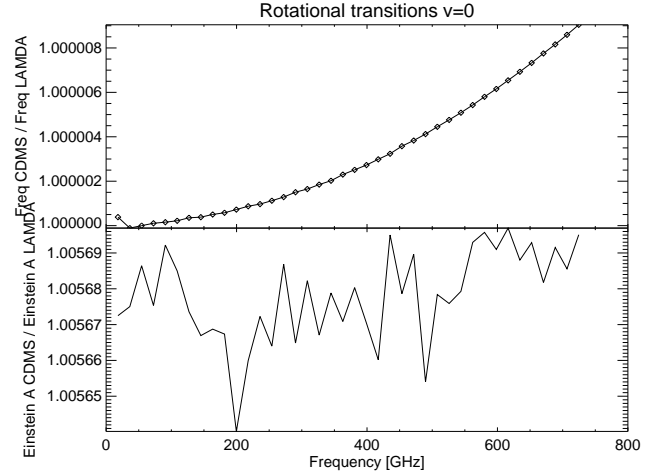


Figure A.3. Comparison between the transition frequencies and Einstein A coefficients of the rotational transitions in the ground state of SiS as listed in the LAMDA database and in the CDMS database.

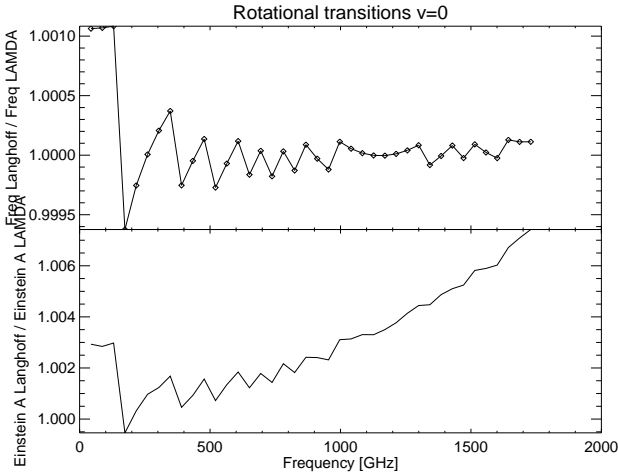


Figure A.2. Comparison between the transition frequencies and Einstein A coefficients of the rotational transitions in the ground state of SiO as listed in the LAMDA database and computed by Langhoff & Bauschlicher (1993).

SiS – silicon monosulfide. Frequencies, transition probabilities and energy levels were taken from the Cologne Database for Molecular Spectroscopy (CDMS, Müller et al. 2005). Transitions in the ground and first vibrational state were included up to $J = 40$. The pure rotational transitions of silicon monosulfide ($^{28}\text{Si}^{32}\text{S}$) and its rare isotopic species have been observed in their ground state as well as vibrationally excited states by employing Fourier transform microwave (FTMW) spectroscopy by Müller et al. (2007). The LAMDA database only lists the lowest 40 levels in the ground vibrational state, for which the energy levels, transition frequencies and Einstein A coefficients were taken from the JPL catalog (Pickett et al. 1998). The values listed in the JPL and CDMS database show good correspondence (see Fig. A.3). As for SiO, the collisional rates for the rotational transitions in the ground state are taken from LAMDA, the collisional rates in the first vibrational state are assumed to be equal to the ones in the ground state, while the vibra-rotational collisional rates are assumed to be zero.

CS – carbon monosulfide. Since the LAMDA database only lists the 41 lowest levels in the ground state (up to $J = 40$, as extracted from the CDMS database), the level energies, frequencies and Einstein A coefficients for the first vibrational state up to rotational quantum number $J = 40$ and the vibra-rotational transitions between $v = 1$ and $v = 0$ were extracted from CDMS. The collisional rates are taken from the LAMDA database and are treated as in the case of SiO and SiS.

CN – cyanogen, cyanide radical, $^2\Sigma^+$. Transition rates for rotational transitions in the ground vibrational state of the cyanide radical are extracted from the CDMS catalog. The CN energy levels are indicated by three rotational quantum numbers: N being the total rotational quantum numbers excluding electron and nuclear spin, J the total rotational angular momentum including electron spin, and F designating the spin quanta. All energy levels with $N_{\text{up}} \leq 39$ are included, yielding 235 energy levels and 508 transitions. For lack of anything better, we have applied the H_2 -CS collisional deexcitation rates from the LAMDA database (Black & van Dishoeck 1991; Hogerheijde & van der Tak 2000). The typical deexcitation rates are estimated not to be in error by more than factors 2–3 (Black & van Dishoeck 1991).

HCN – hydrogen cyanide. A plethora of vibrational states of the HCN molecule are of relevance for astronomical observations. The states are designated by $(\nu_1\nu_2\nu_3)$. The (100) mode is the CH stretching mode at 3311.5 cm^{-1} ; the (010) mode is the doubly degenerate bending mode at 712.0 cm^{-1} ; and the (001) mode is the CN stretching mode at 2096.8 cm^{-1} . The excitation analysis includes radiative excitation through the stretching mode at $3\text{ }\mu\text{m}$ and the bending mode at $14\text{ }\mu\text{m}$. The stretching mode at $5\text{ }\mu\text{m}$ includes transitions that are about 300 times weaker and is therefore not included in the analysis. In each of the vibrational levels, we include rotational levels up to $J = 29$. Hyperfine splitting of the rotational levels were included only in the $J = 1$ levels, where the splitting is larger than the local turbulent width. l -type doubling in the $14\text{ }\mu\text{m}$ transitions was included. Data used are from Schöier et al. (2007c).

SO – sulfur monoxide, $X^3\Sigma^-$. While both the JPL and CDMS database (and hence also the LAMDA database for which the values were extracted from the JPL catalog) list the rotational transitions in the $v = 0$ and $v = 1$ vibrational state, the transition probabilities for the vibra-rotational transitions could not be found. We therefore have restricted the excitation analysis to the first 70 levels in the ground vibrational state as given by the LAMDA database. We note that the collisional rates as given by the LAMDA database are only listed in the range between 50 and 350 K, and no extrapolations to higher temperatures are provided. In case of temperatures in the envelope being higher than 350 K, the rotational rates at $T = 350$ K were used.

SO₂ – sulfur dioxide. Energy levels, frequencies, Einstein A coefficients and collisional rates are taken from the LAMDA database (where they were extracted from the JPL database). The first 198 levels in the ground state are included in the analysis. We note that the collisional rates are taken from Green (1995) and were calculated for temperatures in the range from 25 to 125 K including energy levels up to 62 cm^{-1} for collisions with He. This set of collisional rate coefficients, multiplied by 1.4 to represent collisions with H₂, was extrapolated in the LAMDA database to include energy levels up to 250 cm^{-1} and for a range of temperatures from 10 to 375 K.

H₂O – water. The radiative transfer modeling includes the 45 lowest levels in the ground state and first vibrational state (i.e. the bending mode $\nu_2 = 1$ at $6.3\ \mu\text{m}$). Level energies, frequencies and Einstein A coefficients are extracted from the high-accuracy computed water line list by Barber et al. (2006), currently being the most complete water line list. E.g. while the LAMDA database lists 158 transitions between the 45 lowest levels in the ground state, the line list of Barber et al. (2006) contains 164 transitions. The Einstein A coefficients for the common transitions agree within $\sim 40\%$ (see Fig. A.4).

The H₂O-H₂ collisional rates in the ground state are taken from the H₂O-He rates by Green et al. (1993), corrected by a factor 1.348 to account for collisions with H₂. Rotational collision rates within the first excited state are taken to be the same as for the ground state, while collisions between the ground ν_0 and first excited state ν_2 are based on the ground state rotational collision rate coefficients scaled by a factor 0.01 (Deguchi & Nguyen-Q-Rieu 1990). In their analysis, Deguchi & Nguyen-Q-Rieu (1990) show that the uncertainties in the vibrational collisional rates have no effect on the calculated H₂O lines.

In Sect. 5.3, we compare the H₂O line profile predictions using the Barber and LAMDA line list and the effect of excluding the $\nu_2 = 1$ bending mode and including the asymmetric stretching mode $\nu_3 = 1$ is discussed.

Acknowledgements. We thank I. Cherchneff for useful discussion on the circumstellar non-TE chemistry, and F. Schöier for providing us with an updated HCN linelist in the LAMDA database. LD acknowledges financial support from the Fund for Scientific Research - Flanders (FWO). EDB acknowledges support from the FWO under grant number G.0470.07. H.S.P.M. is very grateful to the Bundesministerium für Bildung und Forschung (BMBF) for financial support aimed at maintaining the Cologne Database for Molecular Spectroscopy, CDMS. This support has been administered by the Deutsches Zentrum für Luft- und Raumfahrt (DLR). The computations for this research have been done on the VIC HPC Cluster of the KULeuven. We are grateful to the LUDIT HPC team for their support.

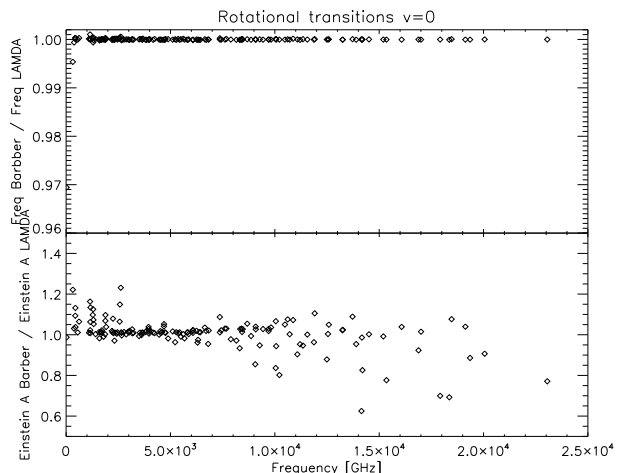
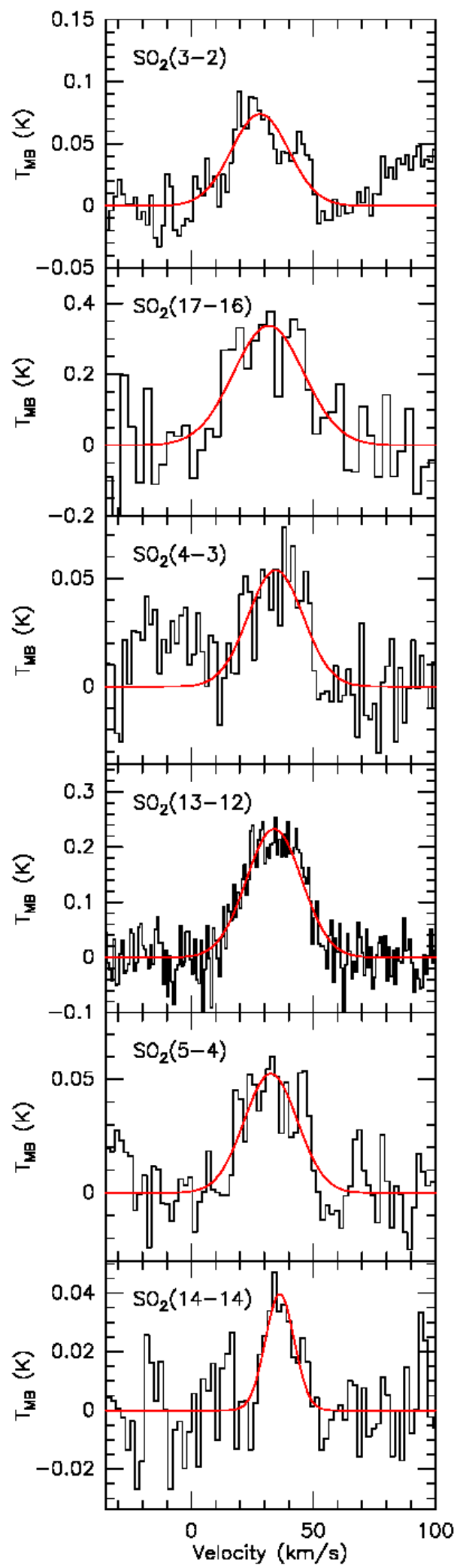


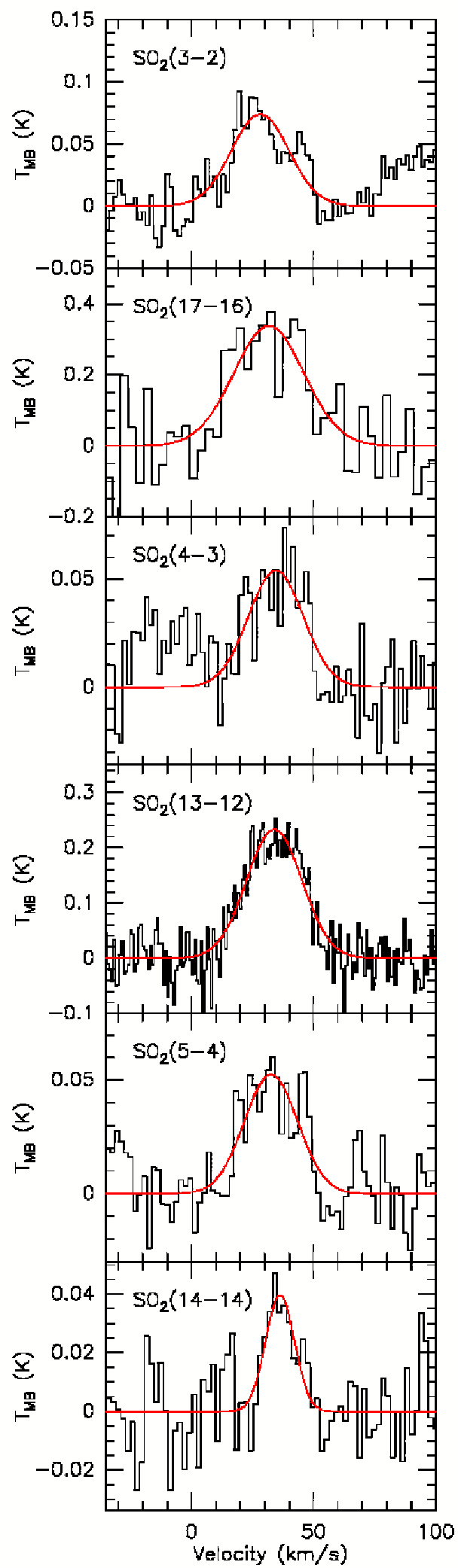
Figure A.4. Comparison between the transition frequencies and Einstein A coefficients of the rotational transitions in the ground state of H₂O as listed in the LAMDA database and as computed by Barber et al. (2006).

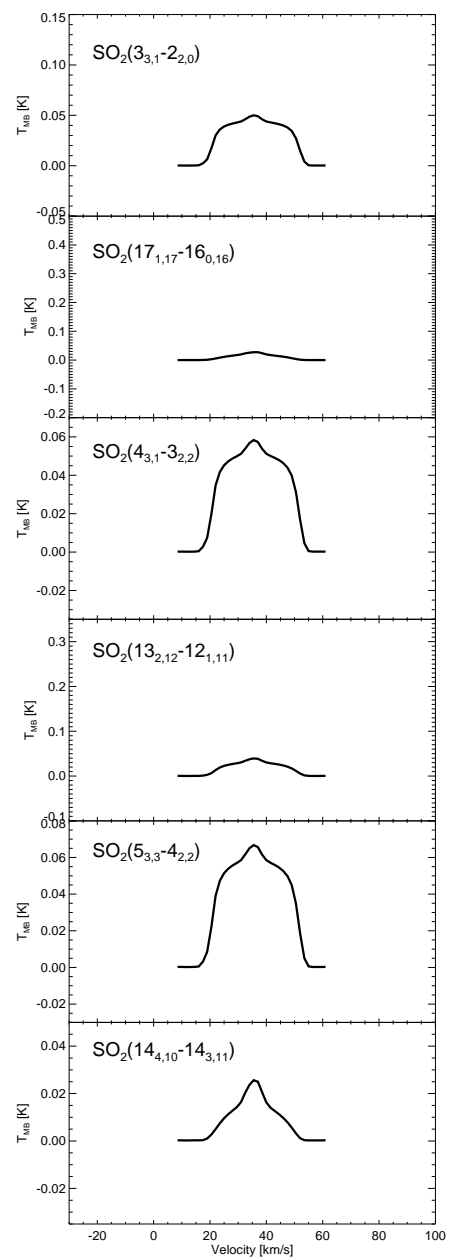
References

- Bachiller, R., Fuente, A., Bujarrabal, V., et al. 1997, *A&A*, 319, 235
 Bains, I., Cohen, R. J., Louridas, A., et al. 2003, *MNRAS*, 342, 8
 Barber, R. J., Tennyson, J., Harris, G. J., & Tolchenov, R. N. 2006, *MNRAS*, 368, 1087
 Biegging, J. H., Shaked, S., & Gensheimer, P. D. 2000, *ApJ*, 543, 897
 Biegging, J. H. & Tafalla, M. 1993, *AJ*, 105, 576
 Black, J. H. & van Dishoeck, E. F. 1991, *ApJ*, 369, L9
 Boboltz, D. A. & Diamond, P. J. 2005, *ApJ*, 625, 978
 Bowers, P. F., Johnston, K. J., & de Vegt, C. 1989, *ApJ*, 340, 479
 Bujarrabal, V. & Alcolea, J. 1991, *A&A*, 251, 536
 Bujarrabal, V., Fuente, A., & Omont, A. 1994, *A&A*, 285, 247
 Bujarrabal, V., Gomez-Gonzales, J., & Planesas, P. 1989, *A&A*, 219, 256
 Carlström, U., Olofsson, H., Johansson, L. E. B., Nguyen-Q-Rieu, & Sahai, R. 1990, in *From Miras to Planetary Nebulae: Which Path for Stellar Evolution?*, ed. M. O. Mennessier & A. Omont, 170
 Cernicharo, J., Guélin, M., & Kahane, C. 2000, *A&AS*, 142, 181
 Cherchneff, I. 2006, *A&A*, 456, 1001
 Crosas, M. & Menten, K. M. 1997, *ApJ*, 483, 913
 De Beck, E., Decin, L., de Koter, A., et al. 2010, *A&A*, *submitted*
 Decin, L., Blomme, L., Reyniers, M., et al. 2008a, *A&A*, 484, 401
 Decin, L., Cherchneff, I., Hony, S., et al. 2008b, *A&A*, 480, 431
 Decin, L. & Eriksson, K. 2007, *A&A*, 472, 1041
 Decin, L., Hony, S., de Koter, A., et al. 2006, *A&A*, 456, 549
 Decin, L., Hony, S., de Koter, A., et al. 2007, *A&A*, 475, 233
 Deguchi, S. & Goldsmith, P. F. 1985, *Nature*, 317, 336
 Deguchi, S. & Nguyen-Q-Rieu. 1990, *ApJ*, 360, L27
 Dominik, C., Sedlmayr, E., & Gail, H.-P. 1993, *A&A*, 277, 578
 Duari, D., Cherchneff, I., & Willacy, K. 1999, *A&A*, 341, L47
 Gail, H.-P. & Sedlmayr, E. 1999, *A&A*, 347, 594
 Goldreich, P. & Scoville, N. 1976, *ApJ*, 205, 144
 González-Alfonso, E., Neufeld, D. A., & Melnick, G. J. 2007, *ApJ*, 669, 412
 González Delgado, D., Olofsson, H., Kerschbaum, F., et al. 2003, *A&A*, 411, 123
 Goorvitch, D. & Chackerian, C. 1994, *ApJS*, 91, 483
 Green, S. 1995, *ApJS*, 100, 213
 Green, S., Maluendes, S., & McLean, A. D. 1993, *ApJS*, 85, 181
 Groenewegen, M. A. T. 1994, *A&A*, 290, 531
 Gustafsson, B., Edvardsson, B., Eriksson, K., et al. 2008, *A&A*, 486, 951
 Hale, D. D. S., Bester, M., Danchi, W. C., et al. 1997, *ApJ*, 490, 407
 Hashimoto, M., Nomoto, K., & Shigeyama, T. 1989, *A&A*, 210, L5
 He, J. H., Dinh-V-Trung, Kwok, S., et al. 2008, *ApJS*, 177, 275
 Hogerheijde, M. R. & van der Tak, F. F. S. 2000, *A&A*, 362, 697
 Hoppe, P., Leitner, J., Meyer, B. S., et al. 2009, *ApJ*, 691, L20
 Jewell, P. R., Snyder, L. E., & Schenewerk, M. S. 1986, *Nature*, 323, 311
 Jiang, B. W., Shen, J. J., & Sun, J. 2003, in *Astrophysics and Space Science Library*, Vol. 283, *Mass-Losing Pulsating Stars and their Circumstellar Matter*, ed. Y. Nakada, M. Honma, & M. Seki, 323–325
 Jura, M. 1983, *ApJ*, 267, 647

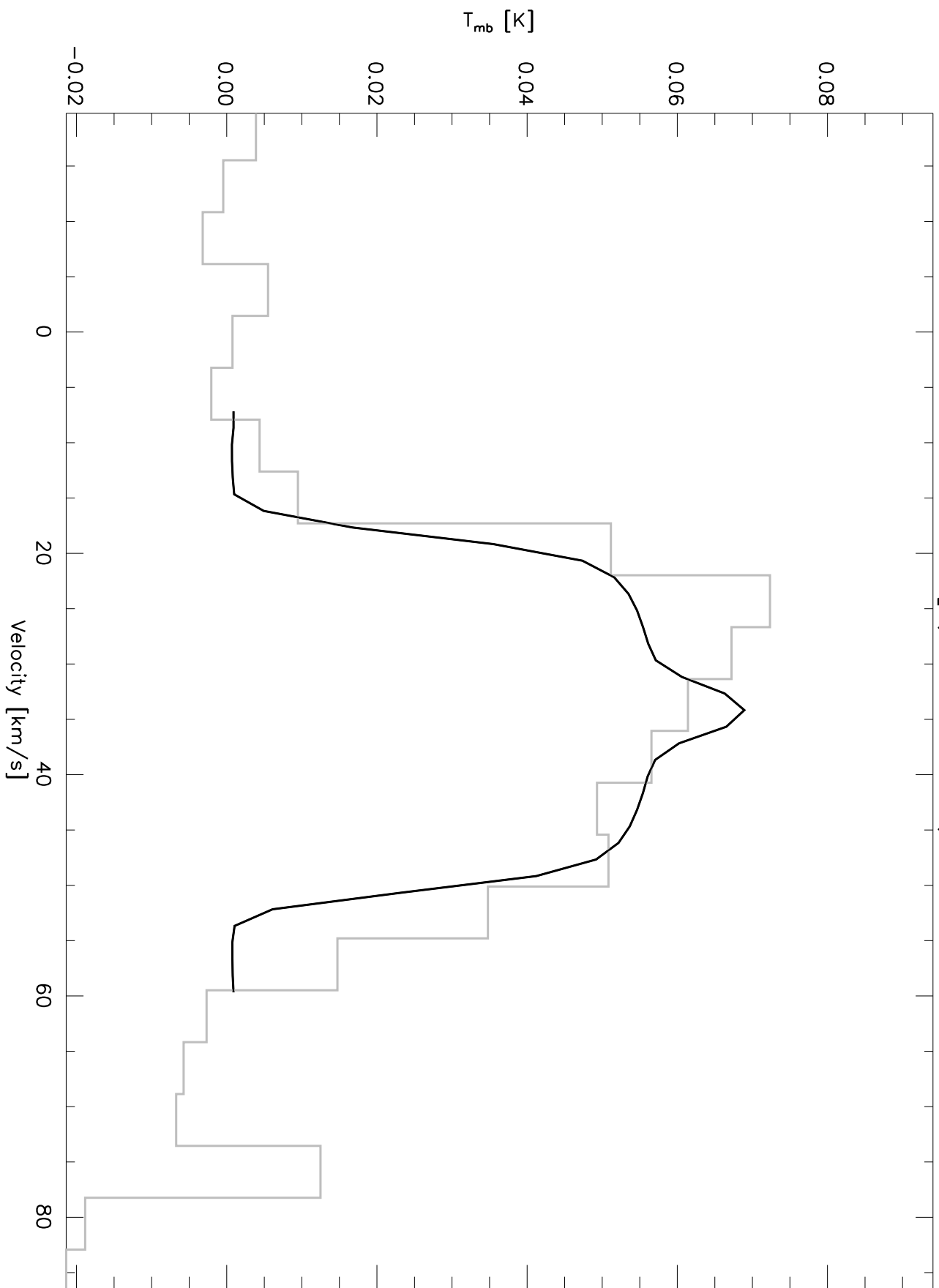
- Justanont, K., Skinner, C. J., & Tielens, A. G. G. M. 1994, *ApJ*, 435, 852
- Kim, H. 2006, Ph.D. Thesis, Universität Bonn, Germany
- Kim, H., Wyroski, F., Menten, K. M., & Decin, L. 2010, *A&A*, *submitted*
- Knapp, G. R. & Morris, M. 1985, *ApJ*, 292, 640
- Lambert, D. L., McWilliam, A., & Smith, V. V. 1987, *Ap&SS*, 133, 369
- Lamers, H. J. G. L. M. & Cassinelli, J. P. 1999, *Introduction to Stellar Winds*, ed. H. J. G. L. M. Lamers & J. P. Cassinelli
- Lane, A. P., Johnston, K. J., Spencer, J. H., Bowers, P. F., & Diamond, P. J. 1987, *ApJ*, 323, 756
- Langhoff, S. R. & Bauschlicher, C. W. J. 1993, *Chem. Phys. Letters*, 211, 305
- Larsson, B., Liseau, R., & Men'shchikov, A. B. 2002, *A&A*, 386, 1055
- Lindqvist, M., Nyman, L.-A., Olofsson, H., & Winnberg, A. 1988, *A&A*, 205, L15
- Loup, C., Forveille, T., Omont, A., & Paul, J. F. 1993, *A&AS*, 99, 291
- Lucas, R., Bujarrabal, V., Guilloteau, S., et al. 1992, *A&A*, 262, 491
- MacGregor, K. B. & Stencel, R. E. 1992, *ApJ*, 397, 644
- Maercker, M., Schöier, F. L., Olofsson, H., et al. 2009, *A&A*, 494, 243
- Maercker, M., Schöier, F. L., Olofsson, H., Bergman, P., & Ramstedt, S. 2008, *A&A*, 479, 779
- Mamon, G. A., Glassgold, A. E., & Huggins, P. J. 1988, *ApJ*, 328, 797
- Marvel, K. B. 2005, *AJ*, 130, 261
- Millar, T. J., Flores, J. R., & Markwick, A. J. 2001, *MNRAS*, 327, 1173
- Molster, F. J., Waters, L. B. F. M., & Tielens, A. G. G. M. 2002, *A&A*, 382, 222
- Mostefaoui, S. & Hoppe, P. 2004, *ApJ*, 613, L149
- Müller, H. S. P., McCarthy, M. C., Bizzocchi, L., et al. 2007, *Physical Chemistry Chemical Physics (Incorporating Faraday Transactions)*, 9, 1579
- Müller, H. S. P., Schlöder, F., Stutzki, J., & Winnewisser, G. 2005, *Journal of Molecular Structure*, 742, 215
- Neri, R., Kahane, C., Lucas, R., Bujarrabal, V., & Loup, C. 1998, *A&AS*, 130, 1
- Netzer, N. & Knapp, G. R. 1987, *ApJ*, 323, 734
- Neugebauer, G., Martz, D. E., & Leighton, R. B. 1965, *ApJ*, 142, 399
- Nittler, L. R., Hoppe, P., Alexander, C. M. O., et al. 1995, *ApJ*, 453, L25+
- Olofsson, H., Lindqvist, M., Nyman, L.-A., & Winnberg, A. 1998, *A&A*, 329, 1059
- Omont, A., Lucas, R., Morris, M., & Guilloteau, S. 1993, *A&A*, 267, 490
- Pickett, H. M., Poynter, I. R. L., Cohen, E. A., et al. 1998, *Journal of Quantitative Spectroscopy and Radiative Transfer*, 60, 883
- Ramstedt, S., Schöier, F. L., Olofsson, H., & Lundgren, A. A. 2008, *A&A*, 487, 645
- Schöier, F. L., Bast, J., Olofsson, H., & Lindqvist, M. 2007a, *A&A*, 473, 871
- Schöier, F. L., Bast, J., Olofsson, H., & Lindqvist, M. 2007b, *A&A*, 473, 871
- Schöier, F. L., Fong, D., Bieging, J. H., et al. 2007c, *ApJ*, 670, 766
- Schöier, F. L., Olofsson, H., & Lundgren, A. A. 2006, *A&A*, 454, 247
- Schöier, F. L., van der Tak, F. F. S., van Dishoeck, E. F., & Black, J. H. 2005, *A&A*, 432, 369
- Schönberg, K. & Hempe, K. 1986, *A&A*, 163, 151
- Sopka, R. J., Olofsson, H., Johansson, L. E. B., Nguyen, Q.-R., & Zuckerman, B. 1989, *A&A*, 210, 78
- Speck, A. K., Barlow, M. J., Sylvester, R. J., & Hofmeister, A. M. 2000, *A&AS*, 146, 437
- Tenenbaum, E. D., Woolf, N. J., & Ziurys, L. M. 2007, *ApJ*, 666, L29
- Teyssier, D., Hernandez, R., Bujarrabal, V., Yoshida, H., & Phillips, T. G. 2006, *A&A*, 450, 167
- Thielemann, F.-K., Nomoto, K., & Yokoi, K. 1986, *A&A*, 158, 17
- Tsuji, T., Ohnaka, K., Hinkle, K. H., & Ridgway, S. T. 1994, *A&A*, 289, 469
- Ukita, N. & Kaifu, N. 1988, in *Lecture Notes in Physics*, Berlin Springer Verlag, Vol. 305, IAU Colloq. 108: Atmospheric Diagnostics of Stellar Evolution, ed. K. Nomoto, 51–+
- van der Tak, F. F. S., Boonman, A. M. S., Braakman, R., & van Dishoeck, E. F. 2003, *A&A*, 412, 133
- Vollmer, C., Hoppe, P., & Brenker, F. E. 2008, *ApJ*, 684, 611
- Willacy, K. & Millar, T. J. 1997, *A&A*, 324, 237
- Wing, R. F. & Lockwood, G. W. 1973, *ApJ*, 184, 873
- Woitke, P. 2006, *A&A*, 460, L9
- Yamamura, I., de Jong, T., Onaka, T., Cami, J., & Waters, L. B. F. M. 1999, *A&A*, 341, L9
- Zinner, E., Nittler, L. R., Gallino, R., et al. 2006, *ApJ*, 650, 350
- Ziurys, L. M., Milam, S. N., Apponi, A. J., & Woolf, N. J. 2007, *Nature*, 447, 1094



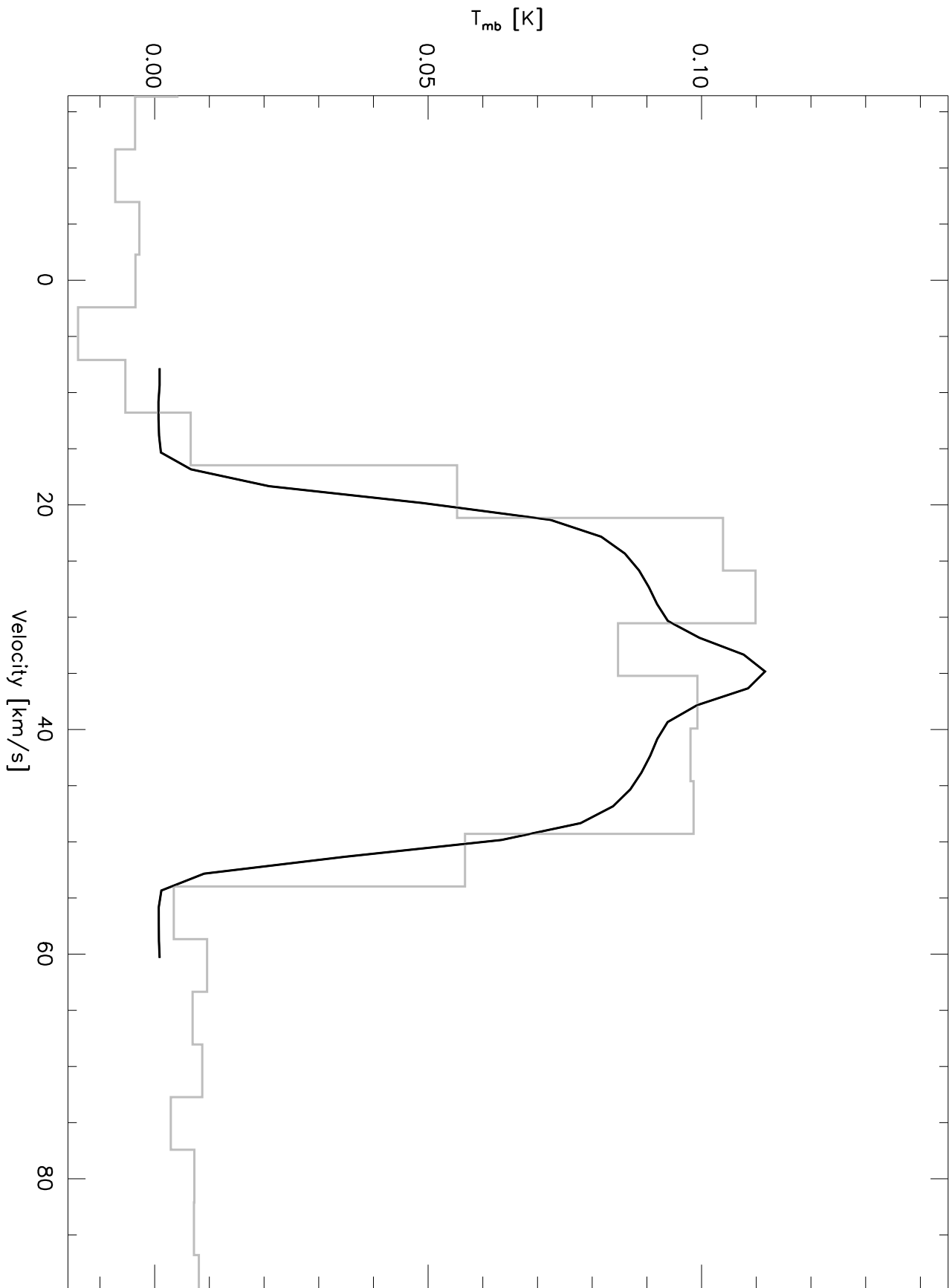




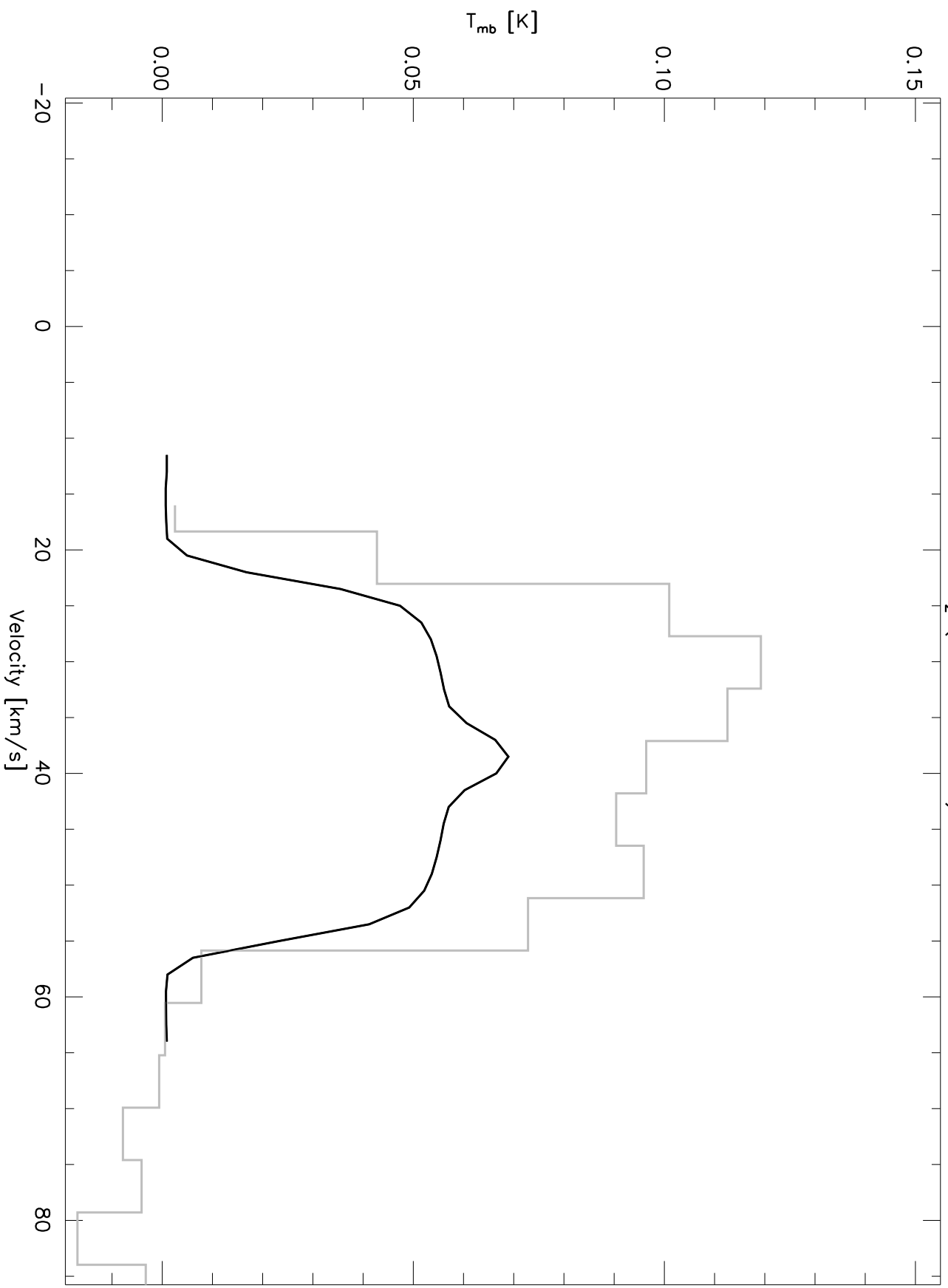
SO₂ (3 3 1 - 3 2 2)



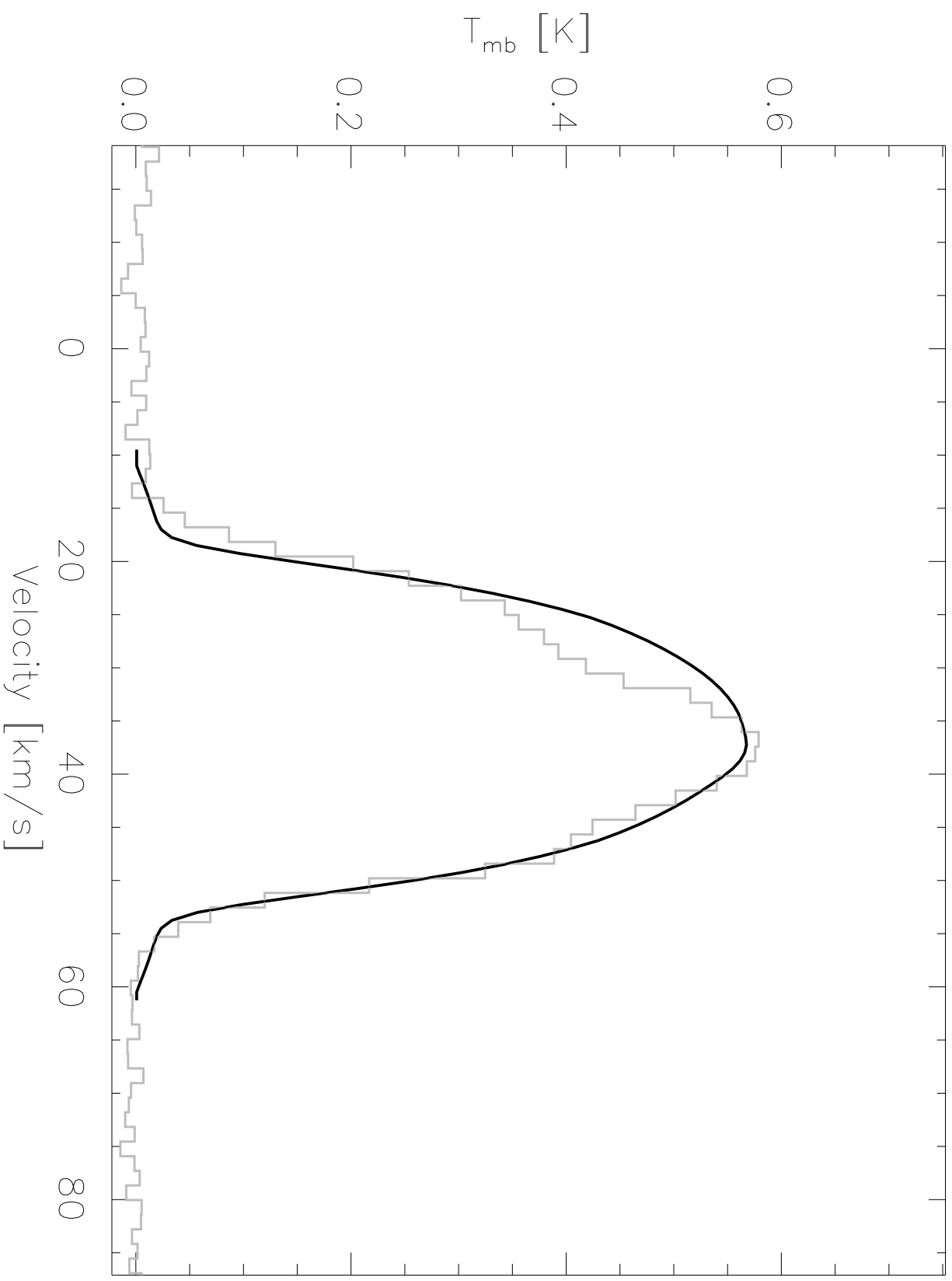
SO₂ (4 3 1 - 4 2 2)



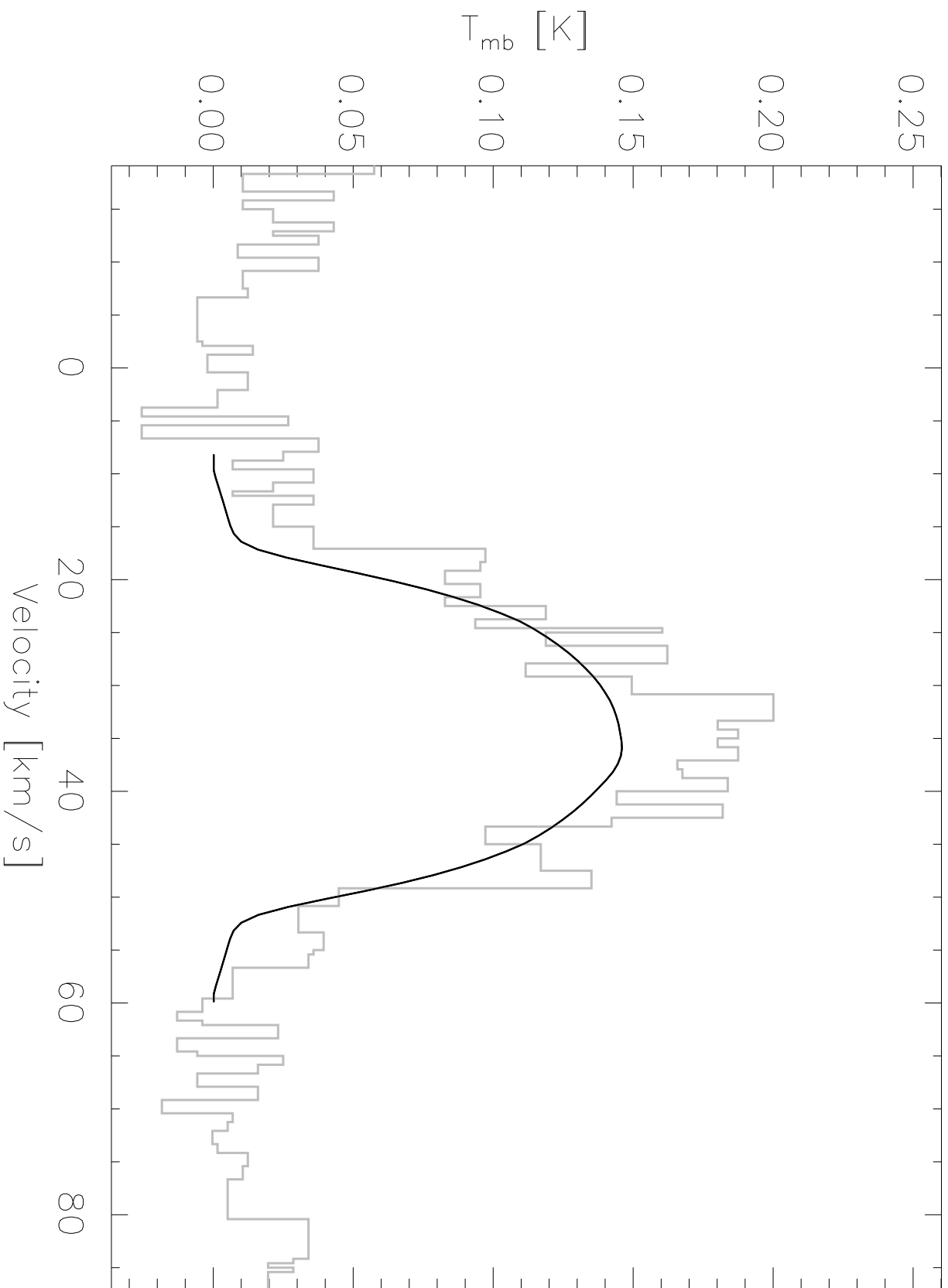
SO₂ (5 3 1 5 2 2)



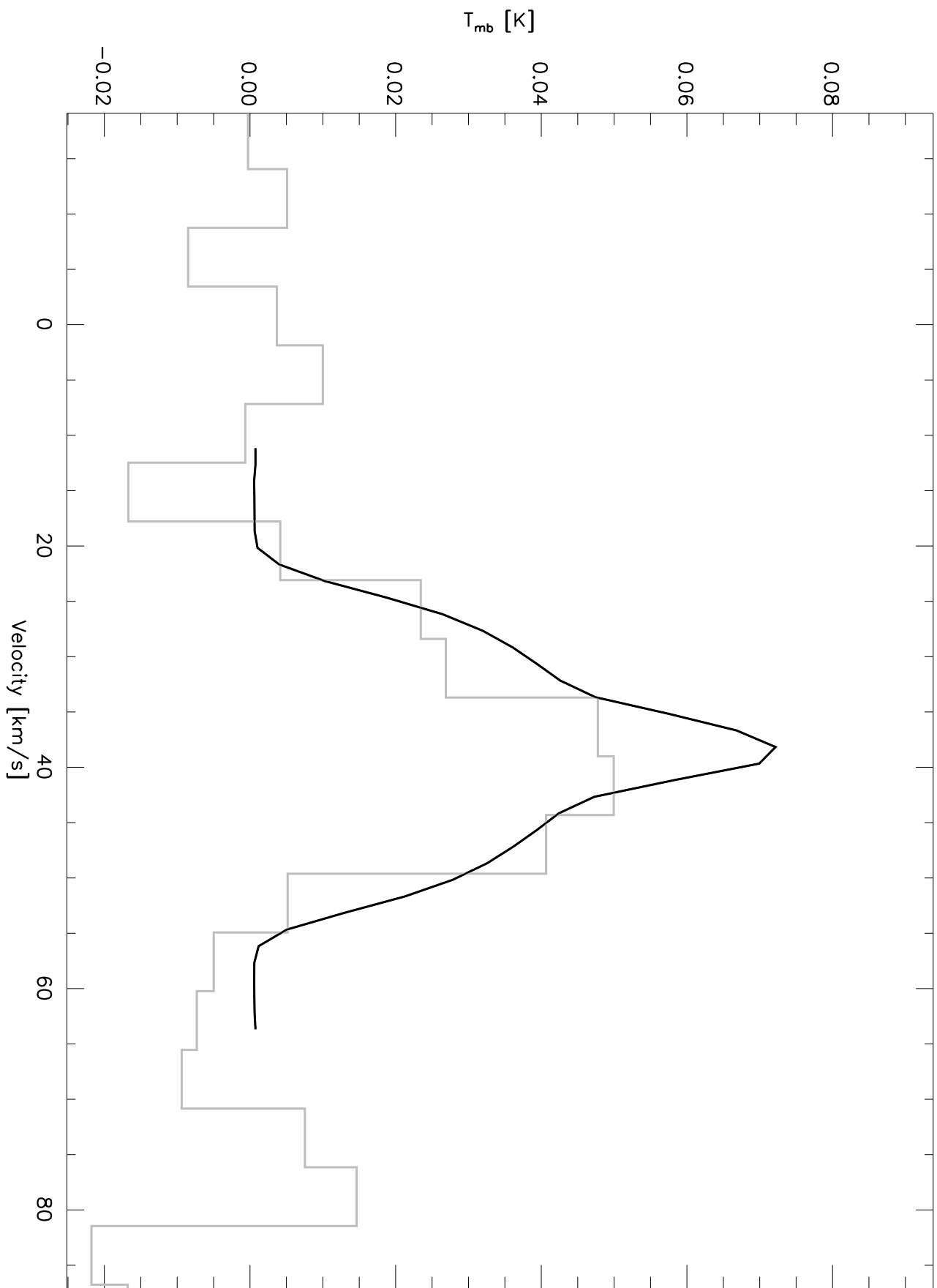
28Si32S(12-11) (IRAM)



28Si32S(12-11) (JCMT)



SO₂ (14 3 11 - 14 2 12)



28Si32S(19-18) (JCMT)

